Chapter-5

Fe_3O_4@L-Arginine and Fe_3O_4@L-Histidine Nanoparticles for One pot Solvent-free Sequential Knoevenagel-Michael Addition Reactions

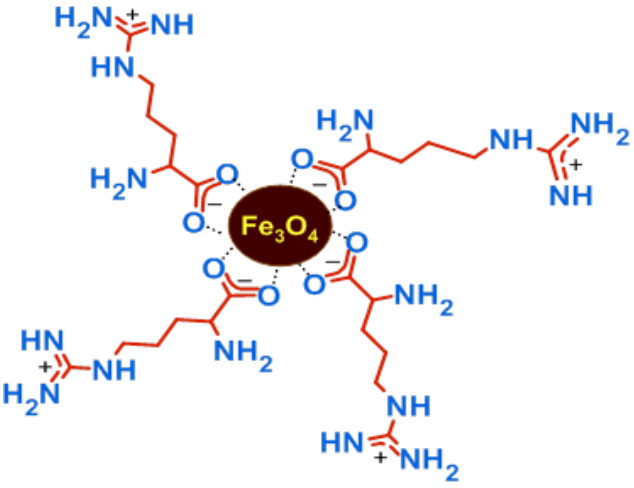

5.1. Introduction

Nowadays, it is difficult to design heterogeneous catalytic one-pot multicomponent reactions (COP-MCRs). For these kinds of reactions to occur, the correct reactants and rea- gents must first be present at a single catalytic site, and then the bond-making and breaking processes must precisely take place in the available spatiotemporal regime, leading to the target product via a stable transition state. Any disturbance during this phase has the potential to alter the outcome of the reaction. The process can be sped up by using a solvent or additive that can stabilize the transition state through H-bonding or electrostatic interactions. The enzyme can accomplish this task effectively in nature. The amino acid residues at the catalytic site in the hydrophobic enzymatic grooves can effectively stabilize the transition state, resulting in the formation of the desired product with no by-products or waste [1]. To synthesize a variety of commercially significant products using green methods, it is necessary to mimic these natural enzymatic processes in the laboratory. To do this, protocols involving MCRs that take place in a single pot either sequentially (known as tandem reactions) or in a cascade (known as dominos reactions) fashion have been developed [2]. Compared to enzyme/homogeneous catalysis, MCRs employing heterogeneous catalysis in organic synthesis have advantages such as greater atom economy, atom usage, and selectivity can be obtained with time, cost, and energy savings [3–6]. Here, we investigated the tandem Knoevenagel–Michael addition events at a single catalytic site, which result in the products possessing a tri-substituted C–C bond in the molecular framework.

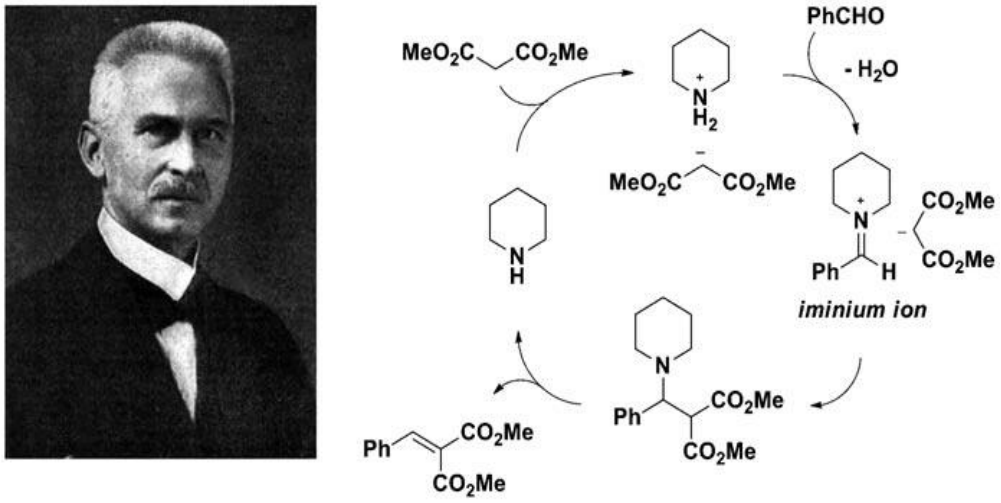

Scheme 5.1. General reaction mechanism for classic Knoevenagel reaction [8].

In a classic Knoevenagel reaction, the nucleophilic addition of a carbanion of an active methylene compound with an electron-withdrawing group to a carbonyl compound is followed by dehydration (Scheme 5.1). This generates trisubstituted alkenes with an E-configuration. A basic mix of piperidine (pKaH 11) and pyridine (pKaH 5.5) is used as a catalyst [7–10].

Alternative catalytic systems were developed to carry out the neat and clean reaction with a smaller value of the E-factor as a consequence of the environmental concerns regarding the basic catalyst mixture. A variety of amino acids, such as -alanine [11], L-proline [12], L-histidine and L-arginine [13] (Scheme 5.2), guanidine [14], Lewis acids, such as $ZnCl_2$ [15], $TiCl_4$ [16], MgF_2 [17], and $CuCl_2$ [18], as well as surfactants, such as benzyl triethylammonium chloride [19], were investigated. Furthermore, heterogeneous catalysts such as organic–inorganic hybrid silica tagged with imidazolium and dihydro imidazolium salts [20], organic amines supported on inorganic solid-acid surfaces [21], silica-L-proline in the liquid phase [22], P4VP/Al_2O_3–SiO_2 [23], $HClO_4$–SiO_2 [24], Ni–SiO_2 [25], modified silica gel [26], magnetic hydroxyapatite-encapsulated γ-Fe_2O_3 nanoparticles [27], MCM-41 [28], MgO/ZrO_2 [29], zeolites [30–34], clays [35] were also employed as catalytic systems. These catalysts have good activity in terms of yield, but high temperature, prolonged reaction times, and catalysts recycling are still problems.

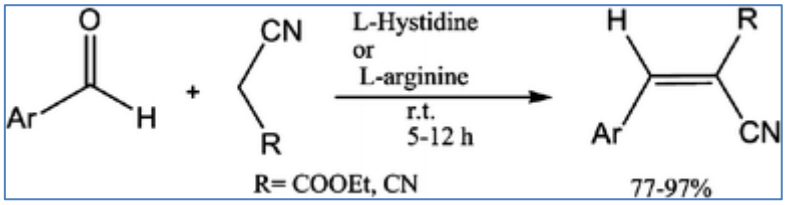

Scheme 5.2. General reported scheme for Knoevenagel condensation reaction [13].

Therefore, the literature review mentioned above stresses the need for the generation of heterogeneous catalysts with the reaction sites basic in nature as well as additional environmental features like recovery and recycling. The best choice in this direction should be iron oxide-based nanoparticles (NPs) capped by amino acid functionalities. Studying the activity of the amino acid in constrained conformations while adsorbed on the magnetic surface might be intriguing. During enzymatic activities, amino acid molecules, and specifically the histidine residue of the enzymes, are known for their proton shuttling. The Knoevenagel reaction involves a similar proton shuttle mechanism [36].

Therefore, it would be preferable to retain the amino acid's molecular conformation and

mimic enzyme-like activity under the reaction conditions. In light of this, we developed iron oxide nanoparticles with L-histidine and L-arginine caps (Fe_3O_4@L-Hist and Fe_3O_4@L-Arg NPs, respectively) for the Knoevenagel reaction.

Now, from the standpoint of the pot economy, it would be advantageous to combine the sequential Michael addition of nitromethane, which is also catalyzed by the same developed base catalytic systems. For the synthesis of several key pharmaceutically important compounds, the Knoevenagel–Michael sequence (KMS) is necessary. The synthesis of (±)-Baclofen (4-amino-3-(4-chlorophenyl) butyric acid) and Pregabalin (Lyrica®) (3-isobutyl-γ-amino butyric acid) are two examples involving KMS. The conventional method for making the basic building blocks of these drugs involves Knoevenagel condensation, 1,4-addition of cyanide, hydrolysis of the resulting β-cyano diester, decarboxylation, reduction, and optical resolution of the resulting racemates (if necessary) (Scheme 5.3) [37].

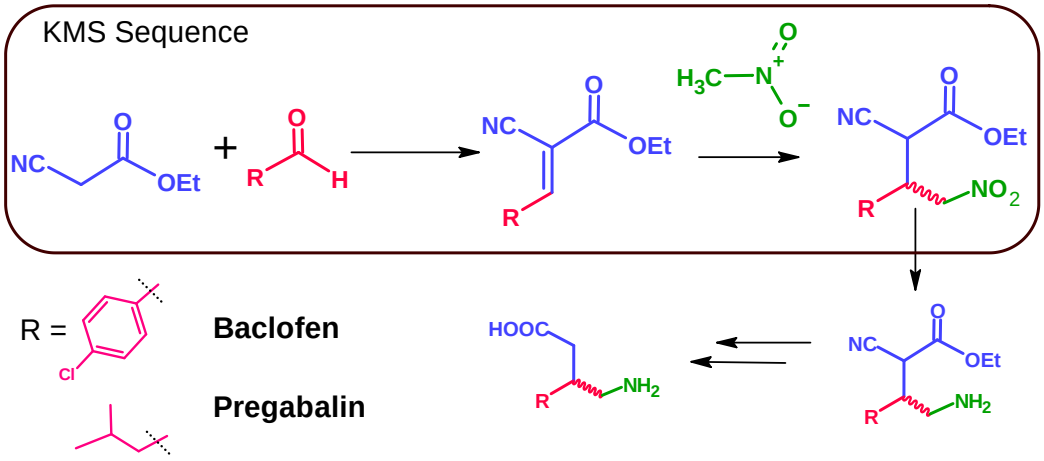

Scheme 5.3. Synthesis scheme involving KMS sequence leading towards pharmaceutically important drugs.

In the current study, we performed one-pot KMS of several aromatic aldehydes in the presence of as-synthesized catalysts under solvent-free conditions, producing precursors of the aforementioned drug molecules. We achieved high conversion and reaction yield in a short time. The catalysts were conveniently removed from the reaction mixture and success fully recycled for up to five cycles.

5.2. Experimental

5.2.1. Material

Ethyl cyanoacetate, 4-nitro benzaldehyde, $FeCl_3$•$6H_2O$, L-histidine, L-arginine, ethyl acetate, and petroleum ether (60–80%) were purchased from Loba Chemie Pvt. Ltd. Benzaldehyde, 4-

chloro benzaldehyde and acetaldehyde were purchased from Spectrochem India. 4-Bromo benzaldehyde, 2-bromo benzaldehyde, 4-methyl benzaldehyde, and 4-methoxy benzaldehyde were purchased from TCI Chemicals (India) Pvt. Ltd. Propionaldehyde was purchased from S. D. Fine Chemical Ltd., India. $FeCl_2.4H_2O$ was purchased from Merck Life Science Private Limited. All the chemicals were used without further purification.

5.2.2. Synthesis of Fe_3O_4@AA NPs

For the preparation of L-arginine coated Fe_3O_4 NPs, $FeCl_3$ anhydrous (0.08 mmol) and $FeCl_2$ (0.04 mmol) were mixed in 50 mL deionized water in a round-bottom flask and the mixture was stirred at 70 °C for 15 min. Then, 10 mL aqueous solution of L-arginine (0.04 mmol) was drop-wise added and the reaction mixture was stirred for 20 min at the same temperature. Then, an aqueous solution of NH_4OH (10.0 mL) was instantly injected and the reaction mixture was stirred at 6000 rpm for 1 h. All the processes were carried out under a nitrogen atmosphere. After that, the resulting material was centrifuged, washed with deionized water and ethanol, and dried at 80 °C in an oven for 12 h. Fe_3O_4@L-histidine NPs were synthesized using the same procedure with L-histidine (0.04 mmol) dissolved in 10.0 mL water.

5.2.3. General procedure for the Knoevenagel condensation reaction

Aldehyde (1.0 mmol), ethyl cyanoacetate (1.0 mmol), and catalyst (80.0 mg) were mixed in the RBF and stirred vigorously at 80 °C in an oil bath. The progress of the reaction was monitored on the TLC plate. After the completion of the reaction, the catalyst was magnetically separated from the reaction mixture. The final isolated product was obtained followed by column chromatography using EtOAc: petroleum ether system.

5.2.4. General procedure for the Michael addition reaction

Nitromethane (2.0 mmol) and catalyst (80.0 mg) were added to the RBF and stirred vigorously at 80 °C. The progress of the reaction was monitored on the TLC plate. After completion of the reaction, the catalyst was magnetically separated from the reaction mixture. The final isolated product was obtained followed by column chromatography using EtOAc:Petroleum ether solvent system.

5.2.5. General procedure for sequential Knoevenagel and Michael addition reaction

In a two necked RBF attached with air condenser and silica-gel guard tube, benzaldehyde (1.0 mmol), ethyl cyanoacetate (1.0 mmol), and Fe_3O_4@L-Arg NPs as catalyst (80.0 mg)

were mixed, and stirred vigorously over the magnetic stirrer. The temperature of the reaction was slowly raised to 80 °C, and the reaction was allowed to continue for 2.5 h at this temperature. Then, nitromethane (2.0 mmol) was injected instantly in the reaction mixture with vigorous stirring. The reaction was continued for further 6 h by maintaining the temperature at 80 °C. Then, the catalyst was separated on applying the magnet outside the RBF, the mixture was decanted followed by column chromatography using EtOAc: petroleum ether solvent system.

5.2.6. General procedure for the recovery of catalyst for sequential Knoevenagel–Michael addition reaction

After completion of the reaction, the catalyst was separated with a magnet and the solvent was evaporated. The recovered catalyst was washed with ethanol and dried and reused under the same conditions as the first run at least 5 times and gave a corresponding product of KMS in high yield and selectivity.

5.3 Results and Discussion

Powder XRD was used to investigate the phase of as-synthesized Fe_3O_4@L-Arg and Fe_3O_4@L-Hist nanoparticles. The magnetite phase is revealed by the diffraction pattern shown in Figure 5.1.

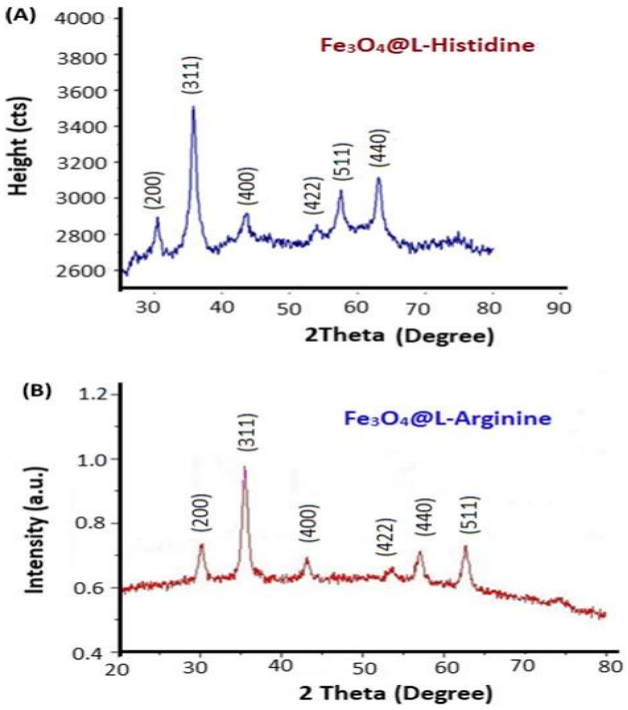

Fig. 5.1. Powder X-ray diffraction patterns of as-synthesized (**a)** Fe_3O_4@L-Hist and (**b)** Fe_3O_4@L-Arg NPs.

The magnetite phase of Fe_3O_4 NPs with inverted spinel structure is confirmed by the X-ray diffraction peaks at 2θ values of 31.0, 36.4, 43.8, 53.5, 57.7, and 63.0°, which, for both systems, correspond to the (220), (311), (400), (422), (511) and (440) planes, respectively (JCPDS No. 82–1533) (Fig. 1).The particle size was determined by the Debye–Scherrer formula ($L = 0.9\lambda/\beta \cos\theta$) and the FWHM (Full Width at Half Maximum) value [38] of the major peak for (311) planes in the range of 20.45 and 16.76 nm, respectively. It can be observed that adsorption of amino acids does not affect the XRD pattern.

Transmission Electron Microscopy (TEM) was used to directly observe the morphology of the sample (Figure 5.2). Figure 2 shows that both catalytic systems Fe_3O_4@ AA (Amino Acids) NPs display spherical morphology in the size range of 2–10 nm. Spherical particles with a crystallite size of 5–10 nm are visible in the HRTEM images. The lattice fringes of the (400) exposed planes are separated by 0.18 nm. The HRSEM images also support these observations.

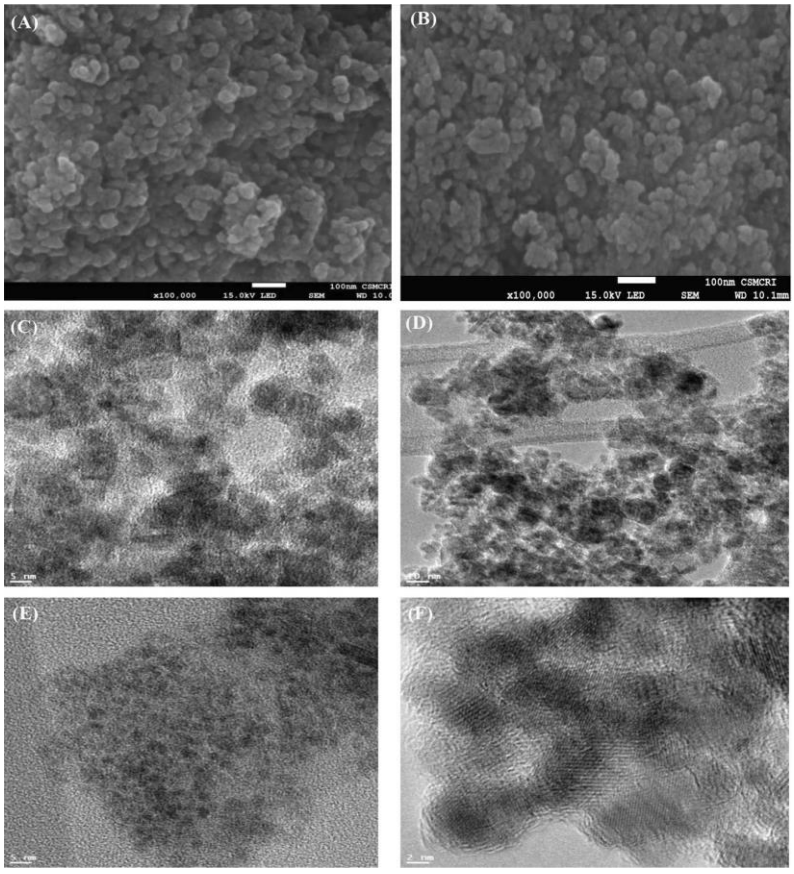

Fig. 5.2. HRSEM images of (**a)** Fe_3O_4@L-Arg (**b)** Fe_3O_4@L-Hist NPs. HRTEM images and lattice fringes at higher magnification of as-synthesized (**c**, **d)** Fe_3O_4@L-Arg and (**e**, **f)** Fe_3O_4@L-Hist NPs.

FTIR spectroscopy is one of the best techniques for investigating the interactions of ligand molecules with the host surface [39–43]. The FTIR spectra of pristine Fe_3O_4, free L-arginine and L-histidine, Fe_3O_4@L-Hist, and Fe_3O_4@L-Arg NPs are presented in Figure 5.9. For pristine Fe_3O_4 NPs, the absorption between 600 and 650 cm^{-1} is due to the Fe–O stretching of the inverse spinel system. The carboxylate ion of the amino acid ligand can coordinate with surface Fe ions in either a mono-dentate or a bidentate (chelating) mode [44, 45]. These can be proven by the COO^- stretching vibration frequencies. Two primary modes of vibration for free carboxylate ions in acetate form are $\nu_{as}(COO^-)$ and symmetric $\nu_s(COO^-)$ stretching at 1583 and 1422 cm^{-1}, respectively. For Fe_3O_4@L-Arg NPs, the ν_{as}(COO-) of carboxylate ions is at 1562 cm^{-1} and $\nu_s(COO^-)$ is at 1472 cm^{-1}. In coordination with surface Fe ions, $\nu_{as}(COO^-)$ decreases while $\nu_s(COO^-)$ increases, indicating that the carboxylate ion of amino acid is coordinated bidentately.

Additionally, Δ ($\nu_{as}(COO^-)$— $\nu_s(COO^-)$) is greater than Δ' ($\nu'_{as}(COO^-) - \nu'_s(COO^-)$), where Δ is the difference between the absorption bands for free carboxylate ions and Δ' for metal-bound carboxylate ions, indicating bidentate coordination [43]. While the ν_{as}(COO-) of carboxylate ions shows at 1588 and $\nu_s(COO^-)$ at 1413 cm^{-1} in the case of Fe_3O_4@L-Hist NPs, suggesting a similar type of bidentate coordination. From the UV–vis spectra, it can be inferred that L-histidine absorbs at 290 nm due to n → π* transition and it fluoresces at 450 nm when excited at the same absorption wavelength which remains unaltered after adsorption on the surface of Fe_3O_4 NPs (Figure 5.9). Based on these investigations, we suggest the bidentate type of amino acid molecule orientations on the surface of magnetic NPs (Figure 5.3). A thermogravimetry analysis of the freshly synthesized NPs was conducted in order to further validate the presence of amino acid molecules adsorbed on the surface. Figure 5.4 shows the thermograms of pristine iron oxide (Fe_3O_4), Fe_3O_4@L-Hist, and Fe_3O_4@L-Arg NPs, which can be utilized for quantification of the material's degradation behavior.

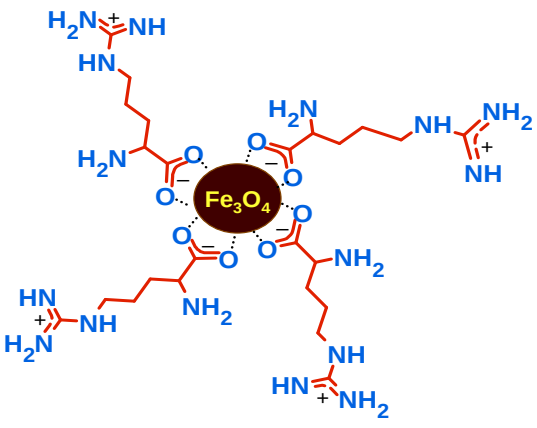

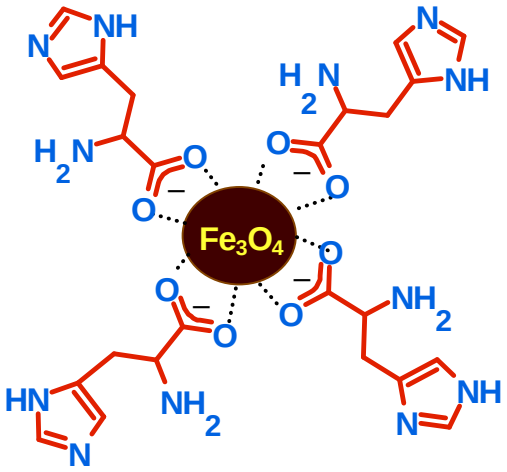

Fig. 5.3. Proposed interaction of L-arginine and L-histidine molecules with the surface of Fe_3O_4 NPs based on FTIR spectroscopy.

In the TG analysis temperature range, iron oxide doesn't lose weight. On the other hand, both of the Fe_3O_4@AA samples exhibit two-stage degradation. Due to the degradation of surface-adsorbed organic material, Fe_3O_4@L-Arg and Fe_3O_4@L-Hist NPs displayed severe weight loss above 150 °C and 150–200 °C, respectively, and persisted up to 400 °C for both samples. The weight loss at around 100 °C is due to the surface-adsorbed water molecules. These studies demonstrate that amino acid molecules are present on the surface of Fe_3O_4 nanoparticles. On the basis of water loss and the %weight of residues left after heat treatment, the loading of L-arginine and L-histidine on the surface of NPs was calculated to be 23.3 and 16.3 percent, respectively.

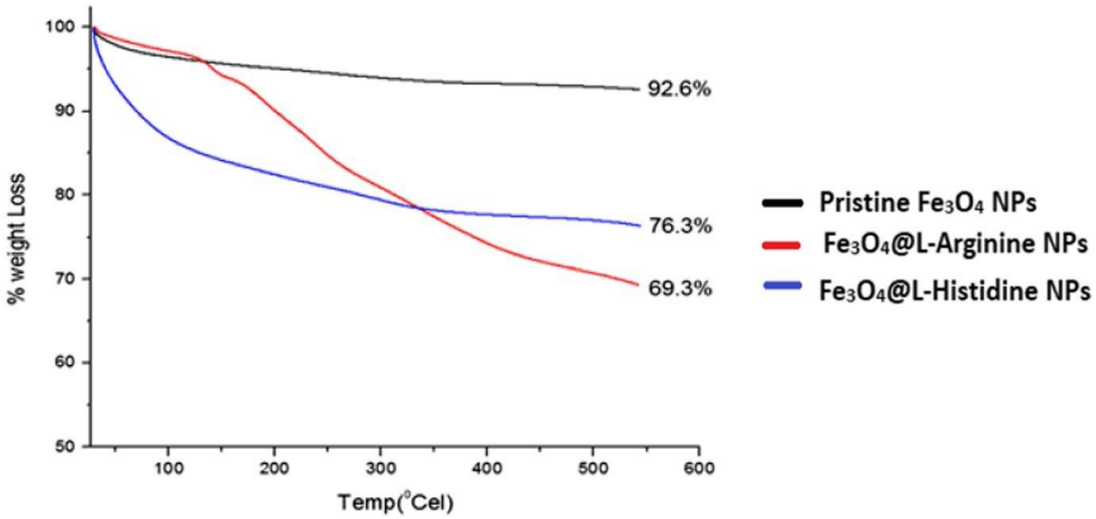

Fig. 5.4. Thermograms of pristine Fe_3O_4, Fe_3O_4@L-Arg, and Fe_3O_4@L-Hist NPs.

The % weight of the residues is mentioned at the end of the curves. The nitrogen adsorption–desorption isotherms for the synthesized Fe_3O_4@L-Arg and Fe_3O_4@L-Hist NPs, as well as their computed BET surface area and pore volume, are shown in Figure 5.5 and Table 1. The isotherms of Fe_3O_4@L-Arg and Fe_3O_4@L-Hist NPs are of type IV (BDDT classification), as seen in Figure 5.5, with the H4 and H3 type of curves, respectively where the two branches are nearly horizontal and parallel throughout a large range of relative pressures (P/Po), suggesting the well-ordered mesoporous structure. In this situation, the amount of gas adsorbed increases as P/Po rises. Narrow pores that resemble slits are frequently linked to the type H4 curve [26, 46]. Fe_3O_4@L-Arg NPs have a much higher surface area than Fe_3O_4@L-Hist NPs, as can be seen in Table 1.

The BET surface area and pore size studies show that both kinds of synthesized NPs systems are good for catalytic activities.

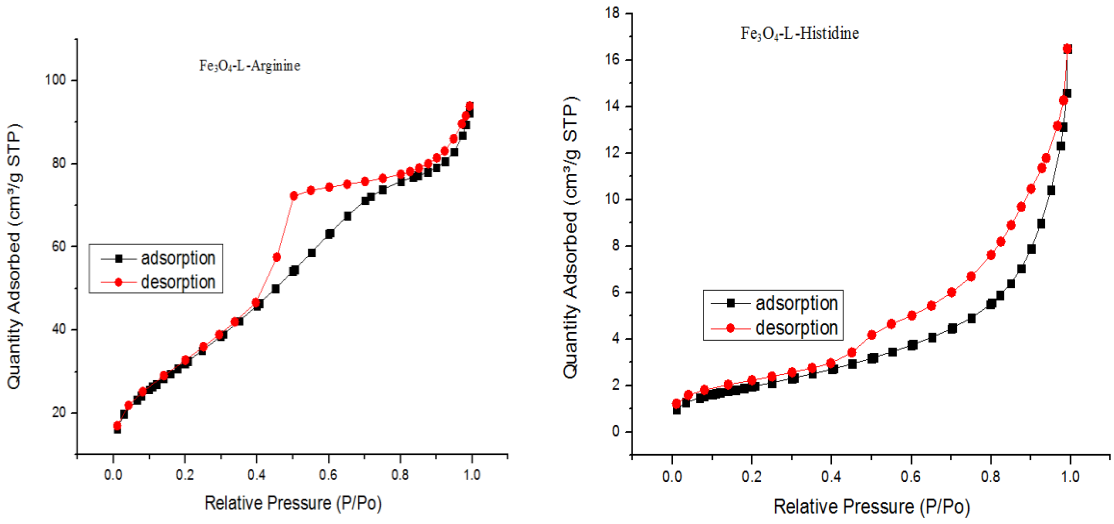

Fig. 5.5. Nitrogen adsorption-desorption isotherms of as-synthesized Fe_3O_4@L-Arg and Fe_3O_4@L-Hist NPs.

Fe_3O_4@L-Arg and Fe_3O_4@L-Hist NPs magnetization curves were plotted using a magnetic field gradient from −15,000 to + 15,000 Oe. As can be seen in Figure 5.6, Fe_3O_4@L-Arg NPs exhibit superparamagnetic behavior with a Ms value of 61.5 emu/g while Fe_3O_4@L-Hist NPs exhibit paramagnetic behaviour with a very low Ms value of 0.25 emu/g [47, 48].

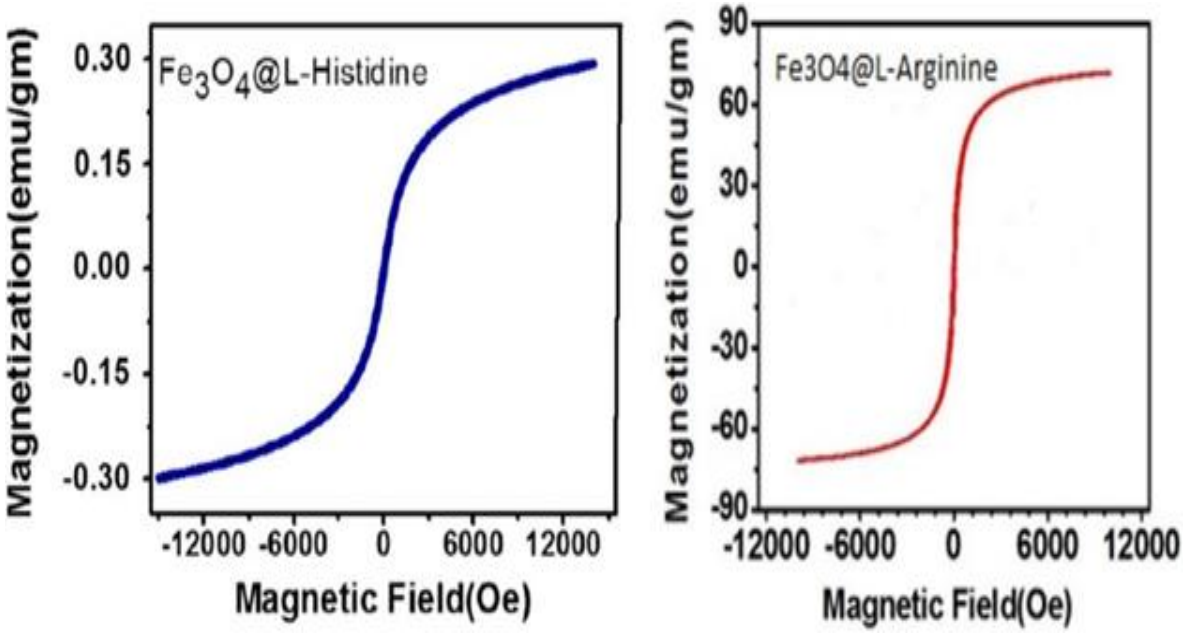

Fig. 5.6. M -H curves for as-synthesized **a** Fe_3O_4@L-Hist and **b** Fe_3O_4@L-Arg NPs

This investigation reveals the material's ability to become magnetized under the influence of a magnetic field and being recovered on removal of the field.

5.4 Optimization of reaction parameters for model Knoevenagel condensation reaction

The model Knoevenagel reaction was carried out under various sets of conditions involving different catalysts, Fe_3O_4@L-Arg or Fe_3O_4@L-Hist, their amounts, sol- vents, and temperature to optimize the reaction parameters. In a model reaction, the Knoevenagel condensation of benzaldehyde (1a) and ethyl cyanoacetate was carried out by using the two as-synthesized catalytic systems. Table 1 shows that the reaction could not continue in the absence of the catalyst. Additionally, we conducted controlled reactions using free L-arginine and L-histidine as well as pristine Fe_3O_4 NPs. Due to the Lewis acidic properties of Fe_3O_4 NPs, the reaction continued in the forward direction with a less yield of the product after 8 h at 80 °C. Due to the solvent-free condition, which is discussed later, the same result was observed when the reaction was conducted in the presence of free amino acids.

Table 1. Effect of different catalysts on Knoevenagel condensation reaction.

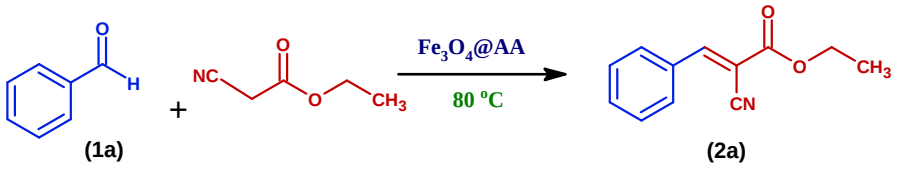

(1a) (2a)

Sr. No.	Catalyst[a]	Yield[a,b] (%)
1	No Catalyst	–
2	Fe_3O_4	17
3	L-Arginine	32c
4	L-Histidine	29c
5	Fe_3O_4@L-Arg	94
6	Fe_3O_4@L-Hist	91

[a]Reaction conditions: Catalyst (80.0 mg), benzaldehyde (1.00 mmol), ethyl cyanoacetate (1.00 mmol), reaction temperature (80 °C), reaction time, 180 min [b]Isolated yield [c]Solvent-less condition

The amount of the catalyst had a significant impact on the reaction. The yield increased dramatically as the catalyst loading was increased, reaching up to 94% in the case of Fe_3O_4@L-Arg on 80 mg of loading (Table 2).

Table 2. Optimization of the amount of catalyst (Fe_3O_4@L-Arg and Fe_3O_4@L-Hist) for the model Knoevenagel condensation reaction.[a,c]

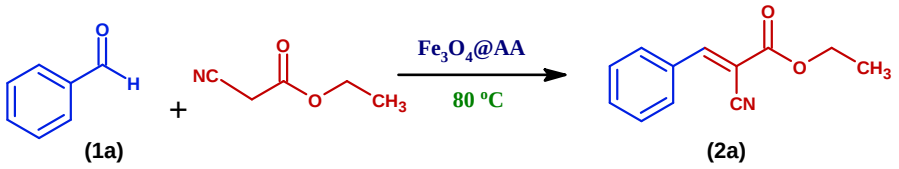

(1a) (2a)

Sr. No.	Catalyst amount (mg)	Yield[b] (%)	
		Fe_3O_4@L-Hist	Fe_3O_4@ L-Arg
1	5.0	43	46
2	10.0	57	59

3	20.0	61	66
4	30.0	74	80
5	50.0	85	89
6	80.0	85	94
7	100.0	85	94

[a]Reaction conditions: benzaldehyde (1.00 mmol), ethyl cyanoacetate (1.00 mmol), reaction time: for Fe_3O_4@L-Hist-180min and Fe_3O_4@L-Arg-150 min, reaction temperature, 80 °C. [b]Isolated yield. [c]Solvent-less condition.

Table 3. Optimization of temperature for Fe_3O_4@L-Arg and Fe_3O_4@L-Hist NPs mediated model Knoevenagel condensation reaction.[a]

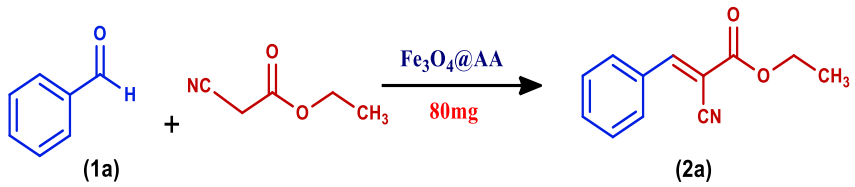

(1a) (2a)

Sr. No.	Temperature (°C)	Yield[b,c] (%)	
		Fe_3O_4@L-Hist	Fe_3O_4@L-Arg
1	10	Trace	Trace
2	RT	39	44
3	40	46	53
4	60	82	91
5	80	85	94

[a]Reaction conditions: Catalyst (80mg), benzaldehyde (1.00 mmol), ethyl cyanoacetate (1.00 mmol), reaction time: for Fe_3O_4@L-Hist-180 min and Fe_3O_4@L-Arg – 150min. [b] Isolated yield. [c] Solvent-less condition.

We tried out a range of temperatures for the model Knoevenagel condensation reaction carried out up to 180 min under the optimized conditions (Table 3). From 10 to 60 °C, the reaction rate was found to be quite slow and then increased with an increase in temperature. At 80 °C, the reaction proceeded with the highest yield.

Time has a substantial impact on the reaction under evaluation. According to (Table 4), for

the Fe_3O_4@L-Arg and Fe_3O_4@L-Hist NPs mediated catalysis, the %yield increased and reached a maximum of 94 and 82% within 150 and 180 min, respectively. For the model Knoevenagel condensation, both of the synthesized catalysts were utilized to evaluate different solvents and solvent-free conditions in order to maximize yield. Table 5 provides an overview of the outcomes. These findings support the notion that for both catalytic systems, solvent-free conditions yield the best outcomes.

Table 4. Optimization of reaction time for Fe_3O_4@L-Arg and Fe_3O_4@L-Hist NPs mediated Knoevenagel condensation reaction.[a,c]

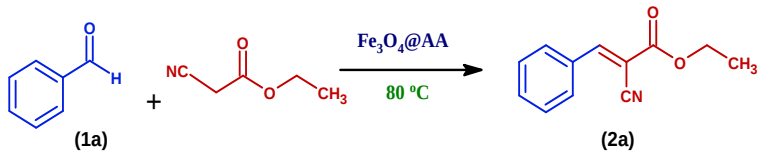

Sr. No.	Time (mins)	Yield[b,c] (%)	
		Fe_3O_4@L-Hist	Fe_3O_4@L- Arg
1	30	20	37
2	60	35	58
3	120	63	79
4	150	71	94[c]
5	180	82	94

[a]Reaction conditions: catalyst (80.0 mg), benzaldehyde (1.00 mmol), ethyl cyanoacetate (1.00 mmol), reaction temperature, 80°C. [b]Isolated yield. [c]Solvent-less condition.

Table 5. Optimization of a solvent system for Fe_3O_4@L-Arg and Fe_3O_4@L-Hist NPs mediated Knoevenagel condensation reaction.[a]

Sr. No.	Solvent	Temperature (°C)	Yield[b] (%)	
			Fe_3O_4@L-Hist	Fe_3O_4@L-Arg
1	Solvent-free	80	91	94
2	Water	80	68	68

3	Ethanol	60	43	43
4	DCM	40	--	--
5	$CHCl_3$	50	10	10

[a]Reaction conditions: catalyst (80.0 mg), benzaldehyde (1.00 mmol), ethyl cyanoacetate (1.00 mmol), reaction temperature, 80°C. [b]Isolated yield. [c]Solvent-less condition.

Table 6. Knoevenagel condensation reaction between aromatic/aliphatic aldehydes and ethyl cyanoacetate catalyzed by Fe_3O_4@L-Arg and Fe_3O_4@L-Hist NPs.[a]

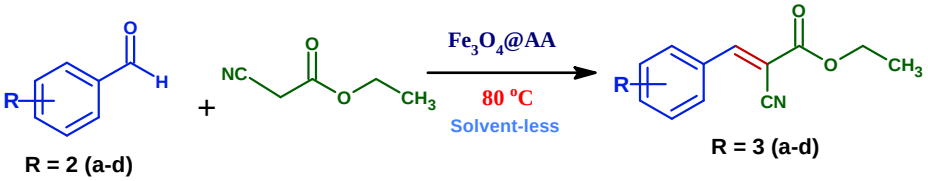

Aldehyde	Product	Time (mins)		Yield[b,c] (%)	
		Fe_3O_4@L-Hist	Fe_3O_4@L-Arg	Fe_3O_4@L-Hist	Fe_3O_4@L-Arg
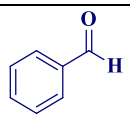 (1a)	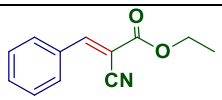 (2a)	180	150	91	94
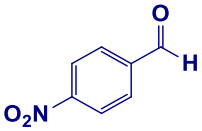 (1b)	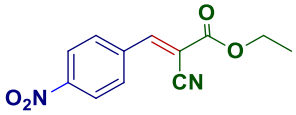 (2b)	75	50	94	97
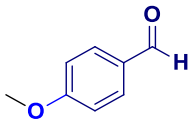 (1c)	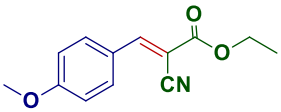 (2c)	180	150	89	90
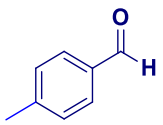 (1d)	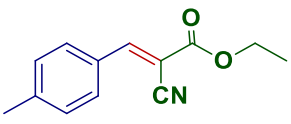 (2d)	180	150	87	89

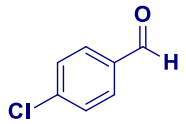 (1e)	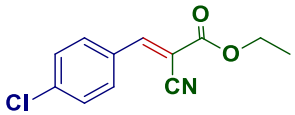 (2e)	90	75	92	95
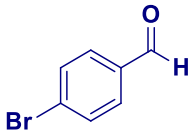 (1f)	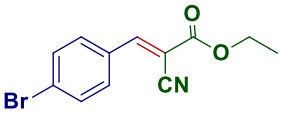 (2f)	90	70	91	93
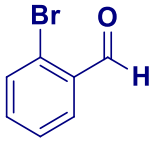 (1g)	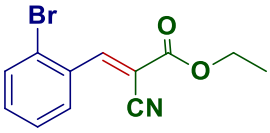 (2g)	90	73	90	91
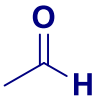 (1h)	--------	180	150	--	--
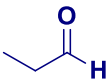 (1i)	--------	180	150	--	--

[a]Reaction conditions: catalyst (80.0 mg), aldehyde (1.00 mmol), ethyl cyanoacetate (1.00 mmol), reaction temperature, 80 °C. [b]Isolated yield. [c]Solvent-less condition.

To comprehend the electronic effects of substituent groups on the reaction, various aromatic and aliphatic aldehydes substituted with electron-donating and withdrawing groups were assessed (Table 6). It was observed that in the case of substituted aromatic aldehydes **1a–g** those with electron-withdrawing groups undergo a faster reaction than with electron-donating groups. In the case of aliphatic aldehydes **1 h-1i**, Knoevenagel condensation did not happen with ethyl cyanoacetate in the presence of catalysts Fe_3O_4@L-Hist and Fe_3O_4@L-Arg under the optimized conditions.

Table 7. Fe_3O_4@L-Arg catalyzed sequential Michael addition reaction with Knoevenagel condensation product.

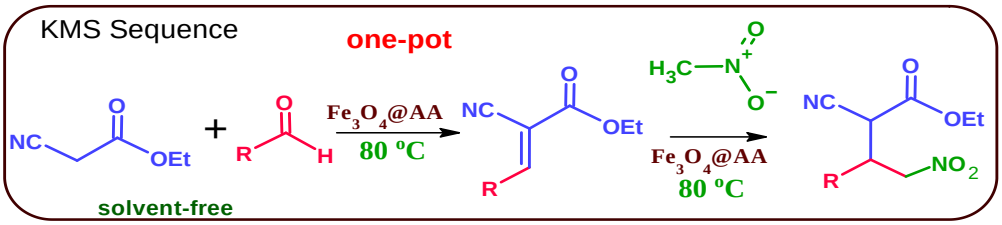

Knoevenagel Adduct	Product	Time (h)	Yield[b] (%)	
			Fe_3O_4@L-Hist	Fe_3O_4@L-Arg
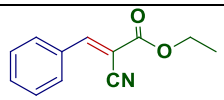 (2a)	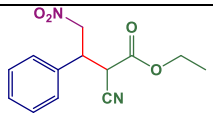 (3a)	6	--	69
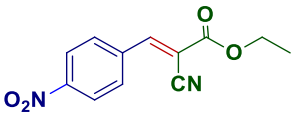 (2b)	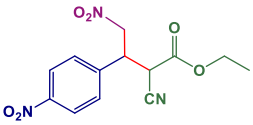 (3b)	5	--	72
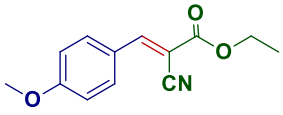 (2c)	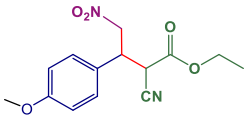 (3c)	5	--	70
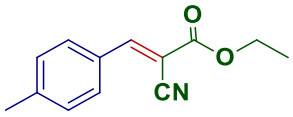 (2d)	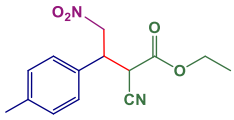 (3d)	6	--	67

[a]Reaction conditions: Catalyst(80.0 mg), Knoevenagelproducts (0.5mmol), Nitro methane(2 mmol), Reaction temperature (80 °C). [b] Isolated yield.

Furthermore, at optimal reaction conditions, Michael addition of Knoevenagel product (2a-d) having electron donating and withdrawing groups was carried out with nitromethane under the optimized reaction parameters. Knoevenagel condensation adduct having electron-withdrawing groups delivered a good yield of Michael product (3a-d) with nitromethane as a

nucleophile compared to electron-donating groups in presence of Fe_3O_4@L-Arg at 80ºC. Fe_3O_4@L-Hist could not catalysed the sequential Michael reaction under the optimized reaction parameters (Table 7).

5.5 Recovery and recycling of Fe_3O_4@L-arginine and Fe_3O_4@L-histidine NPs

Additionally, the model sequential reaction's catalyst recovery was examined under optimal reaction conditions (Figure 5.7). After the KMS reaction was finished, the reaction mixture was filtered and the catalyst was completely washed with ethanol, dried under vacuum at 70°C, and reused for the succeeding reaction cycle.

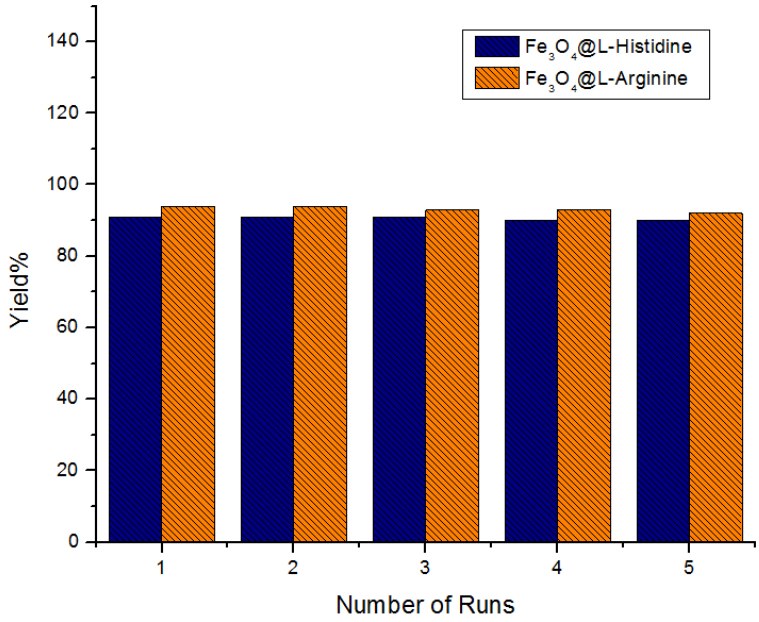

Fig. 5.7. Recovery and recycling study of Fe_3O_4@L-Arg and Fe_3O_4@L-Hist NPs for Knoevenagel reaction.

Under the present conditions, Fe_3O_4@L-Hist (for the Knoevenagel reaction) or Fe_3O_4@L-Arg (for the KMS reaction) can be recovered and reused at least five times. It is significant to notice that after 5 cycles, the catalytic activity is reduced.

Here shows the proposed reaction mechanism based on the review of the literature and the results of the experiments. Consequently, the carboxylate group of the amino acid molecule interacts with the Fe_3O_4 surface Fe^{2+}/Fe^{3+} ions in a bidentate manner, leaving the amine group free (based on FTIR spectroscopy data).

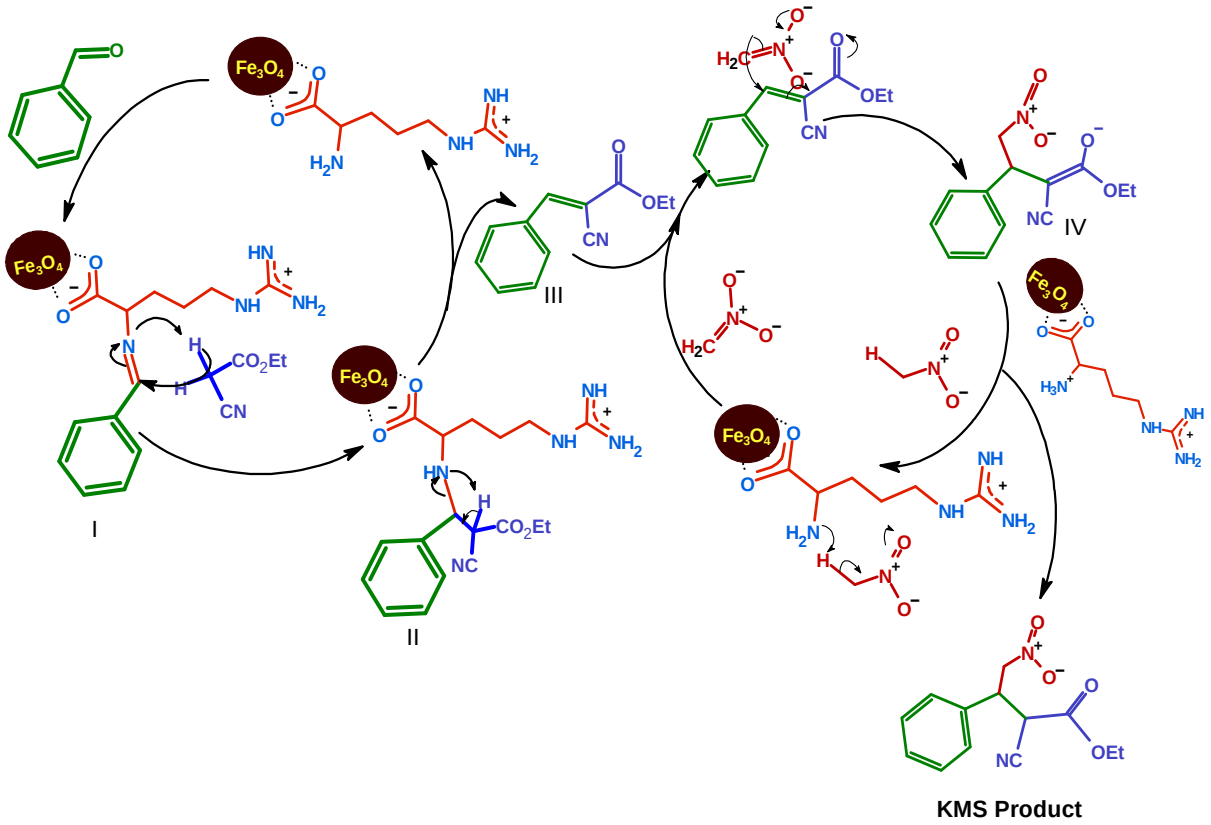

Scheme 5.4. Proposed mechanism for KMS in the presence of Fe_3O_4@L-Arg NPs.

The surface-retained amine group produces imine (**I**) by nucleophilic addition to benzaldehyde. Now, the imine nitrogen atom is sufficiently basic to remove the acidic proton from the ethyl cyanoacetate active methylene group, which in turn initiates the nucleophilic attack of the resultant carbanion to produce the intermediate **II**. Lastly, the base-catalyzed mechanism makes the Knoevenagel product, which is a trisubstituted alkene **III**. Product **III** participates in the sequential Michael reaction as a Michael acceptor, followed by the addition of nitromethane, a Michael donor, which is initiated on the same catalytic site on the magnetic surface (Fe_3O_4@L-Arg) to give the final KMS product (Scheme 5.4).

5.6 Origin of reactivity

In the instance of the Knoevenagel reaction, it can be shown that the Fe_3O_4@L-Arg NPs exhibit stronger catalytic activity than the Fe_3O_4@L-Hist NPs, while the Fe_3O_4@L-Hist NPs catalytic system is completely inactive for the sequential Michael addition process. There could be two major reasons for this. (1) The effective delocalization of the positive charge on the side chain guanidine nitrogen makes L-Arginine more basic than L-histidine. In contrast to the amine group found in the imidazole ring of L-histidine, which has a pKaH of 6.5

(near neutrality), the guanidine amino group of L-arginine has a pKaH of 12. So, during the synthesis of NPs, both of the amino acid molecules get adsorbed and coordinated with surface Fe^{2+}/Fe^{3+} ions by the negatively charged carboxylate group. This happens because the reaction medium is basic due to the ammonia. Now, when these NPs systems are utilised as catalysts under solvent-free conditions, the 1o amino group of L-arginine close to the surface carboxylate ion will be more basic due to the avail- ability of a loan pair of electrons, as the side chain guanidine nitrogen atoms hold the proton more tightly. So, the 1° amine group of L-arginine acts as a basic catalytic site for the reaction under consideration. Instead, the side chain imidazole ring of L-histidine can't hold the basic proton more tightly than that of L-arginine, and the 1° amine of the amino acid near the surface carboxylate ion becomes positively charged at a pH close to neutral [49]. Due to this, L-histidine becomes less basic and is less effective at base catalysis. Hence, it can catalyze the Knoevenagel reaction through the side chain imidazole –NH group but is not basic enough to carry out the sequential Michael addition reaction of nitromethane (Figure 5.8).

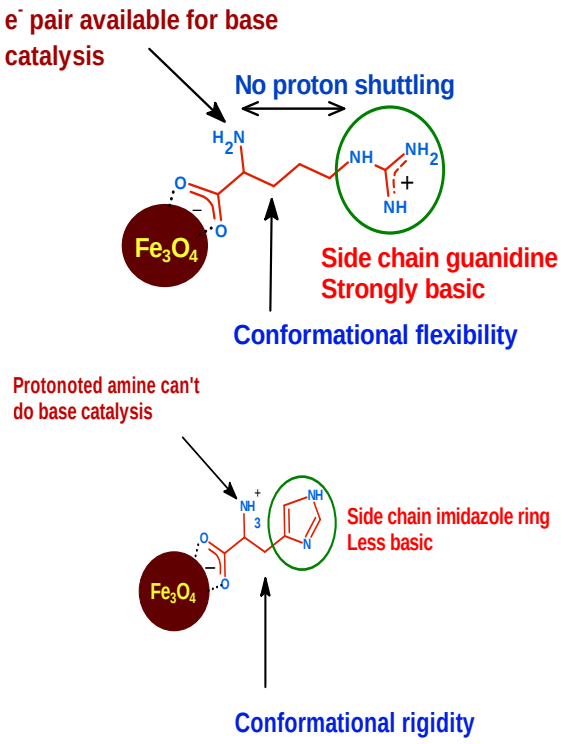

Fig. 5.8. Origin of difference in reactivity of Fe_3O_4@L-Arg and Fe_3O_4@L-Hist NPs catalytic systems.

(2) The flexibility of the adsorbate amino acid molecular framework on the Fe_3O_4 nanoparticle surface. Due to the central three-carbon long "spacer," L-arginine can adopt a better molecular conformation and interact with the substrate aldehyde more easily to form imines, whereas L-histidine could not show reactivity under the optimal conditions because of the rigidity of the molecular framework on adsorption on the magnetic surface (Figure 5.8). Rahmati et al. reported free L-arginine and L-histidine as a catalyst for the Knoevenagel reaction [13]. They condensed various aromatic substituted aldehydes with malononitrile, ethyl cyanoacetate, or ethyl acetoacetate. When the reaction was run in aqueous media for 5–12 h at room temperature, they got good yields. Hence, the "free amino acid" can produce good results when the reaction is conducted "in water," but solvent-free conditions are favored when they are adsorbed on a suitable surface. Table 8 lists the various catalytic systems designed for the Knoevenagel reaction along with their optimized reaction parameters and compares them to the developed NPs systems described in this study.

Table 8. Comparative study of the efficiency of the as-synthesized catalytic systems with those previously reported for the Knoevenagel condensation reaction.

Catalyst	**Substrate**		**Conditions**	**Yield (%)**	**Ref.**
[HyEtPy]Cl–H_2O–DABCO composite	4-Cl-C_6H_4-CHO	Ethyl cyanoacetate	H_2O,50 ^oC, 20 mins	98	[48]
SiO_2-L-proline	4-NO_2-C_6H_4-CHO	Malononitrile	Acetonitrile, 80 ^oC, 7 h	90	[11]
	4-NO_2-C_6H_4-CHO	Ethyl cyanoacetate	Acetonitrile,80 ^oC, 7 h	--[b]	
FeNPs/PPD@rGO	C_6H_5-CHO	Malononitrile	Toluene,40 ^oC, 3.5 h	100	[49]
	C_6H_5-CHO	Ethyl cyanoacetate	Toluene, 40 ^oC,3.5 h	23.7	
SMNPs-Amp	C_6H_5-CHO	Malononitrile	H_2O, RT, 4 h	99	[50]

composite					
Chol-MNPs (com)	C_6H_5-CHO	Ethyl cyanoacetate	Ethanol, RT, 24 h	79	[51]
	C_6H_5-CHO	Malononitrile	Ethanol, RT, 0.5 h	98	
Lys-Chol-MNPs	C_6H_5-CHO	Ethyl cyanoacetate	Ethanol, RT, 24 h	65	[51]
	C_6H_5-CHO	Malononitrile	Ethanol, RT, 0.5 h	96	
Gly-Chol-MNPs	C_6H_5-CHO	Ethyl cyanoacetate	Ethanol, RT, 24 h	67	[47]
	C_6H_5-CHO	Malononitrile	Ethanol, RT, 0.5 h	97	
Fe_3O_4@L-Arginine	C_6H_5-CHO	Ethyl cyanoacetate	Solvent-free, 80 ^oC,150 mins	94	**This work**
Fe_3O_4@L-histidine	C_6H_5-CHO	Ethyl cyanoacetate	Solvent-free, 80 ^oC,180 mins	91	**This work**

[a][HyEtPy]Cl–H_2O–DABCO composite - 1,4-diazabicyclo [2.2.2] octane (DABCO) hydroxyl group in the ionic liquid of N-(2-Hydroxy-ethyl)-pyridinium chloride ([HyEtPy]Cl); SiO_2-L-proline - silica supported L-proline, FeNPs/PPD@rGO-p-phenylenediamine FeNPs (Iron nanoparticles) embedded onto the surface of Graphene nanosheet; SMNPs-Amp composite - (aminomethyl) phenols-modified nano catalysts; Chol-MNPs (com) - silane ligand containing choline hydroxide; Lys-Chol-MNPs - choline hydroxide function was neutralized with Lysine; Gly-Chol-MNPs - choline hydroxide function was neutralized with Glycine. [b] No reaction.

It can be shown that malononitrile is a preferred substrate (because the methylene group may be easily activated by two nearby cyano groups) and that a fair yield can be obtained when it is condensed with aldehydes.

However, there are few reports of ethyl cyanoacetate condensing with aldehydes and the protocols that do achieve a moderate to low yield. According to Table 8, the as-synthesized NPs catalytic system is a productive "green" catalyst for the Knoevenagel condensation reaction when no sol- vent is present. We also used the conventional formula from the literature to compute the E-factor, which we found to be 0.42 for the Fe_3O_4@L-Arg and 0.47 for the Fe_3O_4@L-Hist NPs catalyst systems, respectively [50]. These outcomes render the developed protocol truly "green."

E-Factor calculation for primary amines (as-synthesized in the present study)

Fe_3O_4@L-Arg =(0.1 gm benzaldehyde + 0.113 gm ethyl cyanoacetate + 0.080 gm catalyst)-0.206 gm product / 0.206 gm product = **0.42**

Fe_3O_4@L-Hist = (0.1 gm benzaldehyde + 0.113 gm ethyl cyanoacetate + 0.080 gm catalyst)-0.199 gm product/0.199 gm product = **0.47**

5.7 Conclusion

By introducing amino acid-like components as a base catalyst on a robust host like Fe_3O_4 NPs, we have shown that one-pot multi-step synthesis of pharmaceutically significant intermediate can be carried out sequentially. The Knoevenagel reaction can simply be carried out by base catalysis due to amino acid molecules that are present on the surface of a single nanoparticle. The product of this reaction was then condensed with nitromethane, a Michael donor, yielding a product useful in the production of numerous pharmaceutically active compounds. It can be concluded that by adopting all the optimal process parameters, (i) the developed process becomes more cost-effective than those based on bare noble metal catalysts (ii) catalyst recovery is made simple by using a magnetic field (iii) The catalyst Fe_3O_4@L-Arg is more effective than Fe_3O_4@L-Hist for both sequential reactions (iv) the as-synthesized catalyst Fe_3O_4@L-Arg NPs maintained its efficiency for five cycles (in this study) for 2-way catalysis (v) the reaction is "green" because no hazardous solvents are used, and the entire one-pot process can be carried out in solvent-free conditions with short reaction times, high product yields, and high activity and stability of the catalyst under the optimized reaction conditions. This work brings up new possibilities for the development of multi-component catalysts that can produce materials on a large scale while being environmentally friendly. The next investigation will focus on developing a tandem process for the mass production of enantio-pure Baclofen and Pregabalin.

5.8 Characterization

X-ray powder diffraction (XRD) pattern was obtained using X-ray powder diffractometer (Philips X'pert MPD system) with Cu Kα radiation, λ = 0.15418 nm. The BET-specific surface area (SBET) was determined by nitrogen adsorption (Micro- metrics ASAP 2020, USA) via a multipoint BET method using the adsorption data in the relative pressure (P/Po) range of 0.0–1.0. The samples were degassed at 80 ºC before Brunauer–Emmett–Teller (BET) measurements. Desorption isotherm was used to determine the pore-size distribution using the Barret– Joyner–Halendar (BJH) method, assuming a cylindrical pore model. The nitrogen adsorption volume at the relative pressure (P/Po) range of 0.997 was used to determine the pore volume and average pore size. The morphology of the samples was examined by FESEM (JEOL-JSM-7100F). Particle size with elemental mapping was carried out by TEM (JEOL-JEM-2100) at 200 kV. FT-IR spectra of all compounds were recorded with Bruker FTIR spectrometer using KBr pellets in the range of 400 to 4000 cm^{-1}. UV–visible absorption spectra were recorded on a Perkin Elmer Lambda 35 and PL spectra were recorded on a Jasco FP-6300 spectrophotometer using a Xenon lamp as an excitation source at 280 nm. All measurements were made at 25 °C in methanol. HRMS was recorded on Xevo G2-S Q Tof (Waters, USA), and TG analysis was recorded on Exstar TG/DTA7000 from 30 to 550 °C with a heating rate of 10 °C. The sample size was between 7–8 mg. The ^{1}H NMR and ^{13}C NMR were recorded on Bruker Advance 400 MHz spectrometers using TMS as an internal standard in $CDCl_3$.

5.8.1 FTIR spectra of catalysts

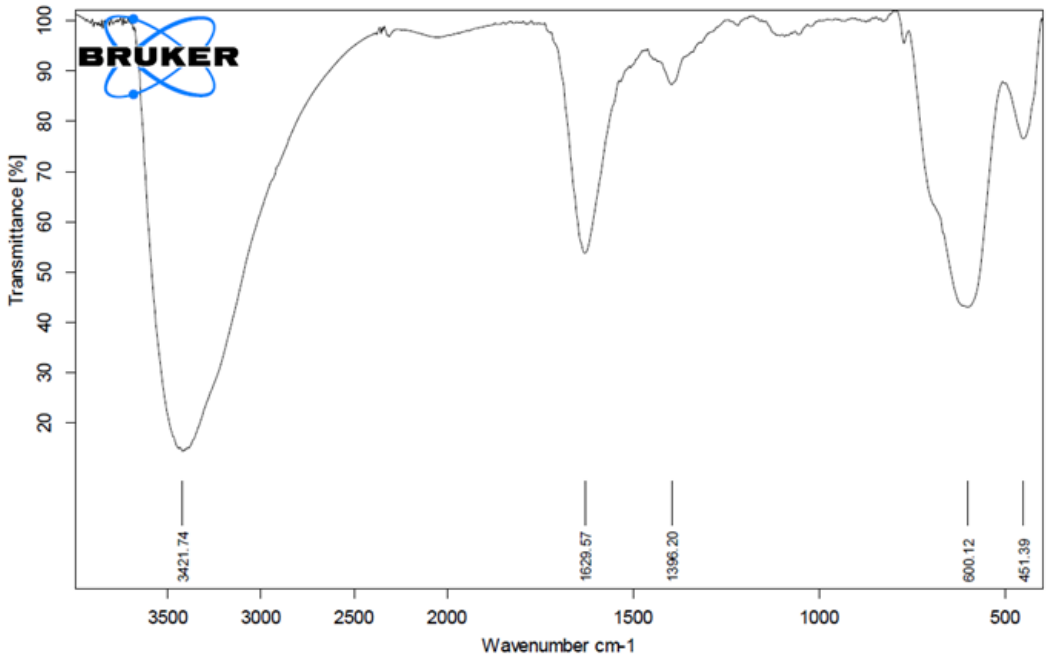

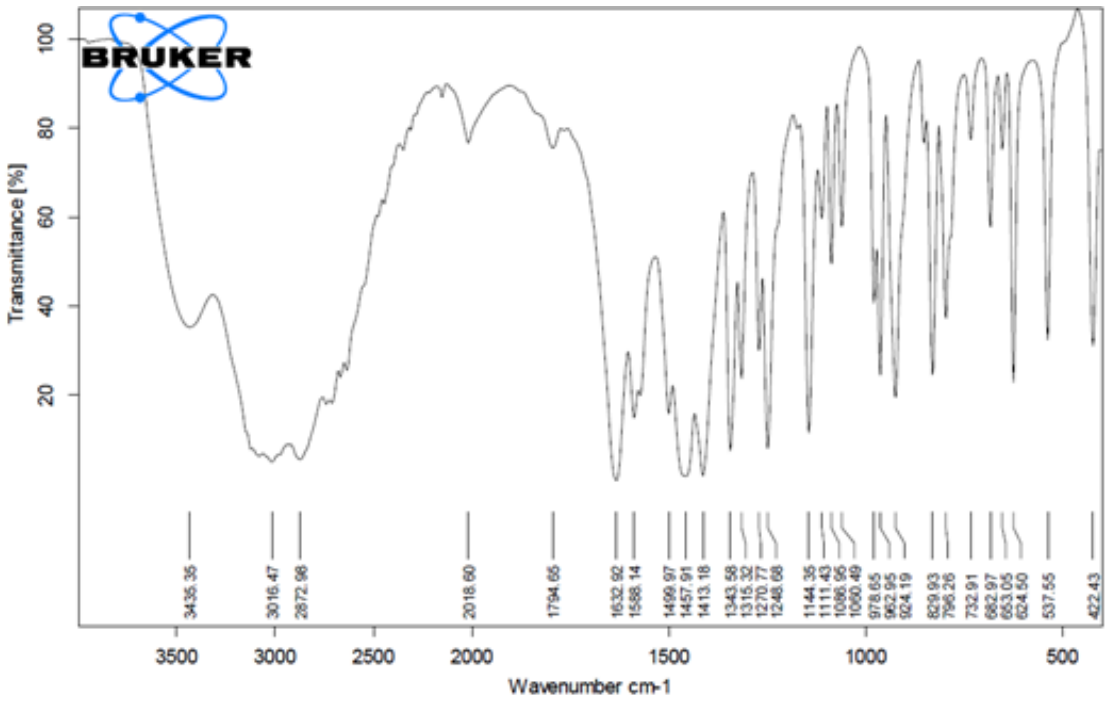

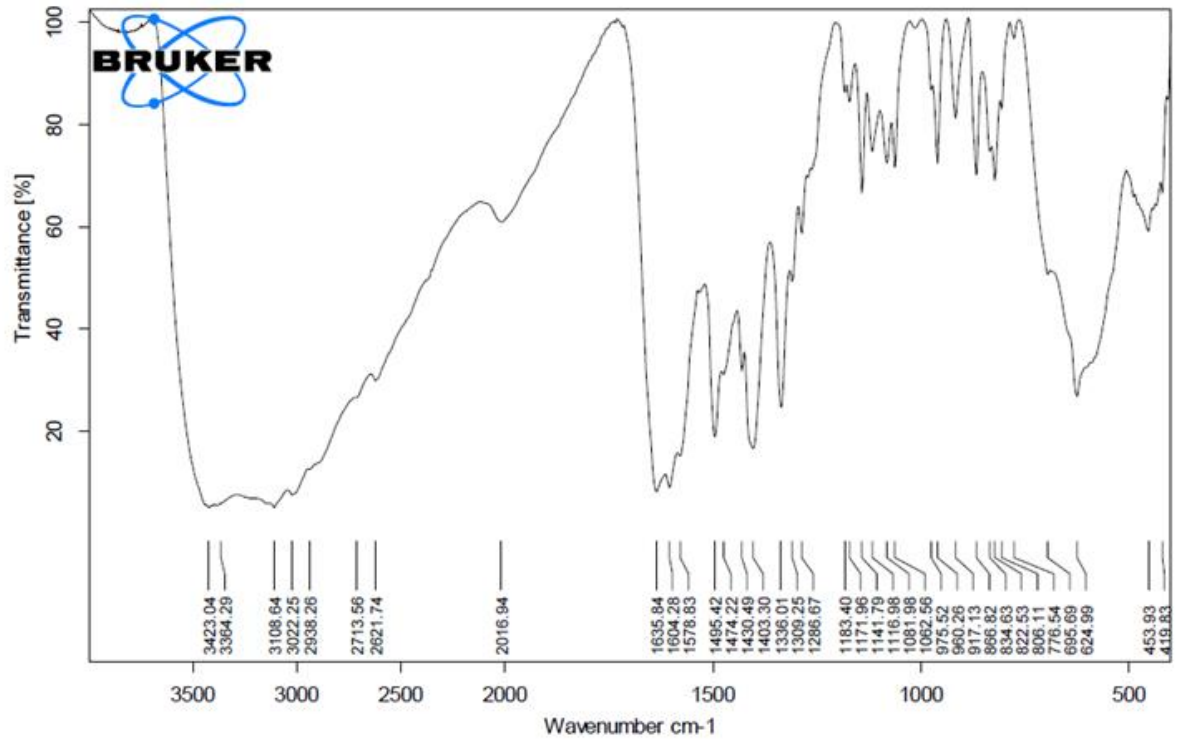
BRUKER
Transmittance [%]
100
80
60
40
20
3423.04
3364.29
3108.64
3022.25
2938.26
2713.56
2621.74
2016.94
1635.84
1604.28
1578.83
1495.42
1474.22
1430.49
1403.30
1336.01
1309.25
1286.67
1183.40
1171.96
1141.79
1116.98
1081.98
1062.56
975.52
960.26
917.13
886.82
834.63
822.53
806.11
776.54
695.69
624.99
453.93
419.83
3500
3000
2500
2000
1500
1000
500
Wavenumber cm-1

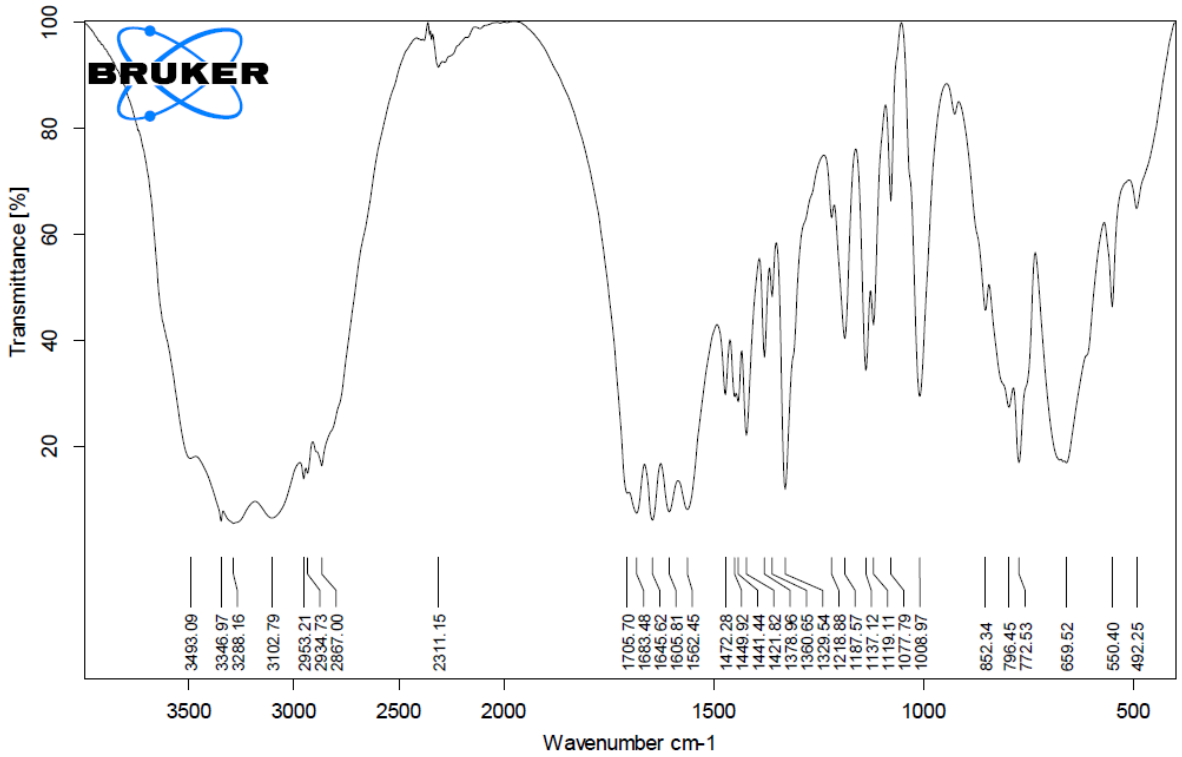
BRUKER
Transmittance [%]
100
80
60
40
20
3493.09
3346.97
3288.16
3102.79
2953.21
2934.73
2867.00
2311.15
1705.70
1683.48
1645.62
1605.81
1562.45
1472.28
1449.92
1441.44
1421.82
1378.96
1360.65
1329.54
1218.88
1187.57
1137.12
1119.11
1077.79
1008.97
852.34
796.45
772.53
659.52
550.40
492.25
3500
3000
2500
2000
1500
1000
500
Wavenumber cm-1

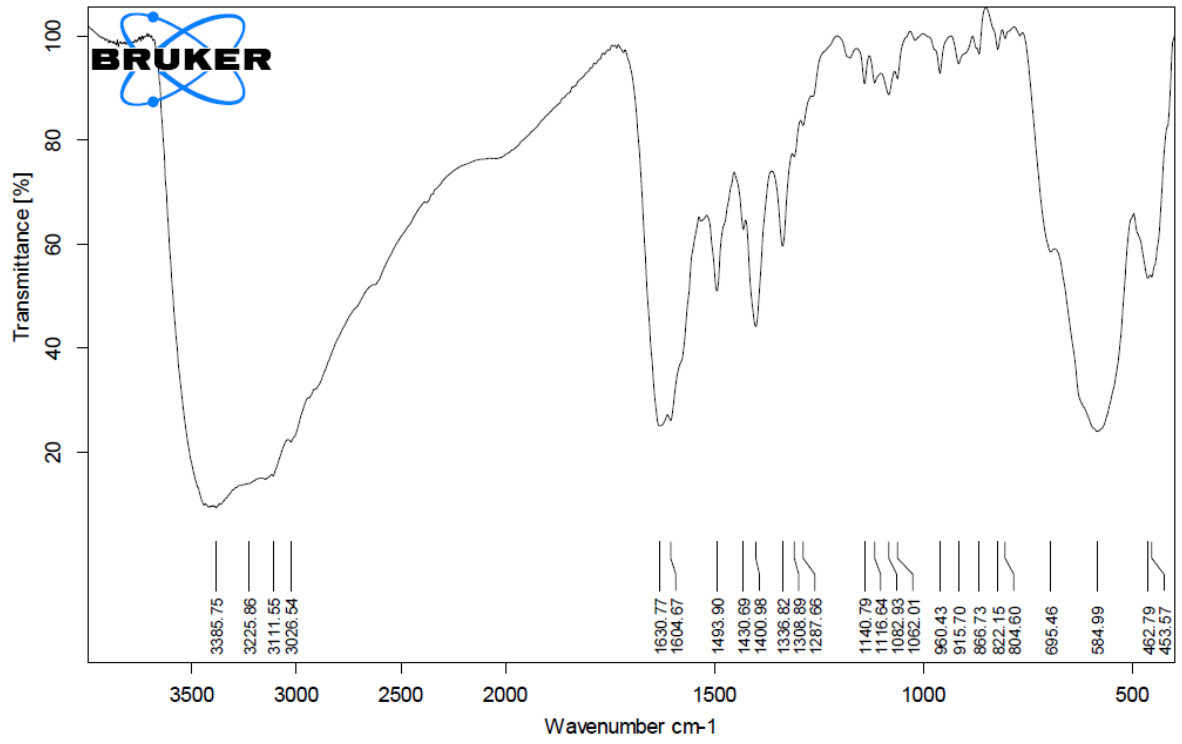

Fig. 5.9. (A) Fe_3O_4 NPs (B) L-Histidine (C) Fe_3O_4@L-Histidine (D) L-Arginine (E) Fe_3O_4@L-Arginine.

5.8.2 UV-vis absorption spectra and emission spectra of the catalysts

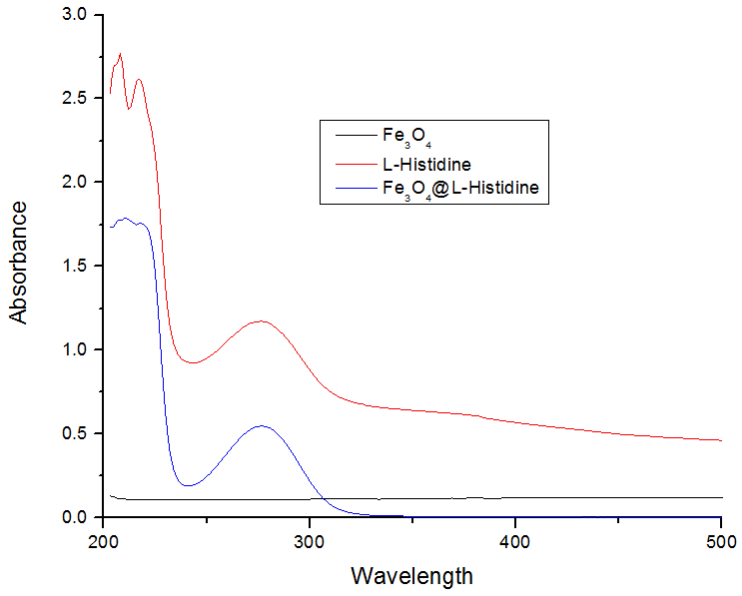

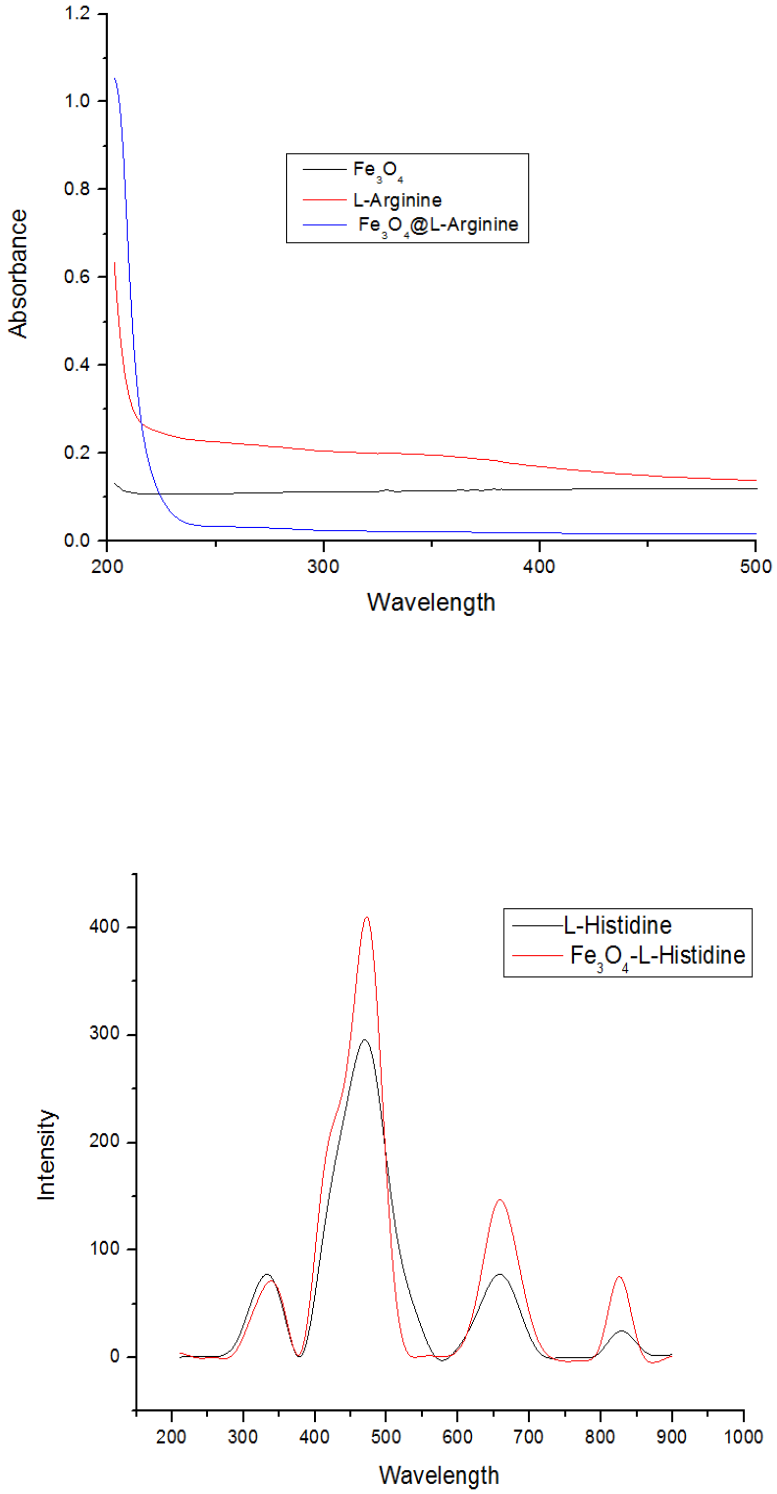

Fig. 5.10. UV-vis absorption spectra of (A)Fe_3O_4@L-Histidine (B) Fe_3O_4@L-Arginine and (C) emission spectra of Fe_3O_4@L-Histidine.

5.8.1 FT-IR, NMR and GC-MS Spectra of the Products

(*E*)-Ethyl- 2-cyano-3-phenylacrylate (2a)

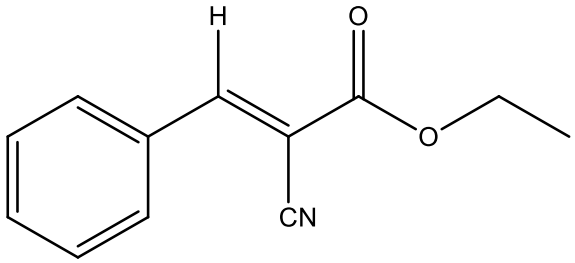

White solid crystals (M.p. 49–51 °C). FTIR (KBr, cm^{-1}). 2981 (–C–H, stretching, sp^2), 2939 (–C–H, stretching, sp^3), 2222 (–CN), 1726 (–C=O ester), 1606 (–C=C), 1444–15,720 (–C=C, Ar). ^{1}H NMR (400 MHz, $CDCl_3$) δ: 1.43 (CH_3, t, J = 7.2 Hz, 3H), 4.42 (CH_2, q, J = 7.2 Hz, 2H), 7.49–7.59 (ArH, m, J = 7.2 Hz, 3H), 7.99–8.01 (ArH, d, J = 8.4 Hz, 2H), 8.27 (–CH, s, 1H). ^{13}CNMR (400 MHz, $CDCl_3$) δ: 14.2 (–CH_3), 62.8(–O–CH_2), 102.9 (–C–CN), 115.5 (–CN), 129.3, 131.1, 131.5, 133.4, 155.1, 162.5 (–C=O). ESI–MS (m/z) = 201.2 $[M + H]^+$ (Figure 5.11—5.14).

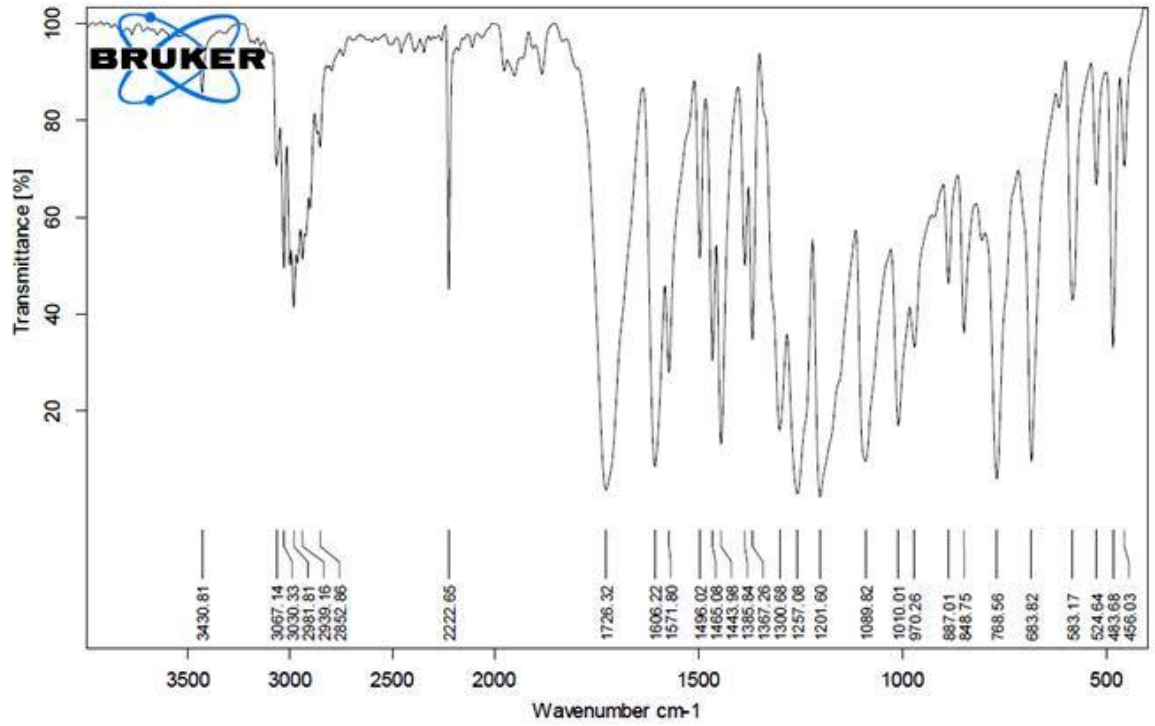

Fig. 5.11. FT-IR spectra of the product (2a).

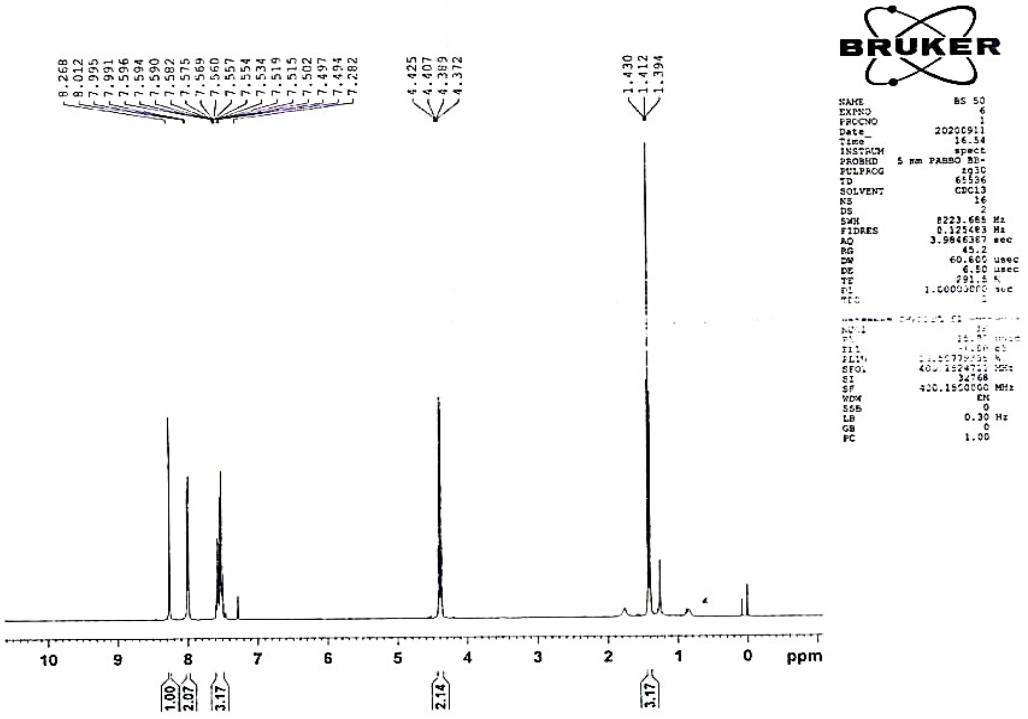

Fig. 5.12. ^{1}H NMR spectra of the product (2a).

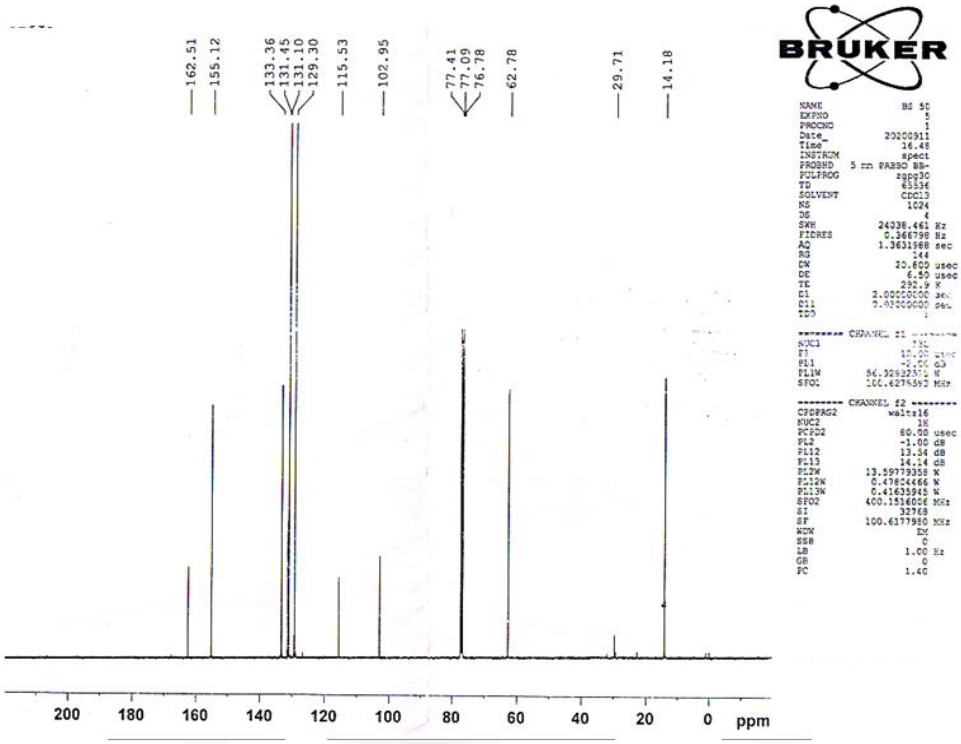

Fig. 5.13. ^{13}C NMR spectra of the product (2a).

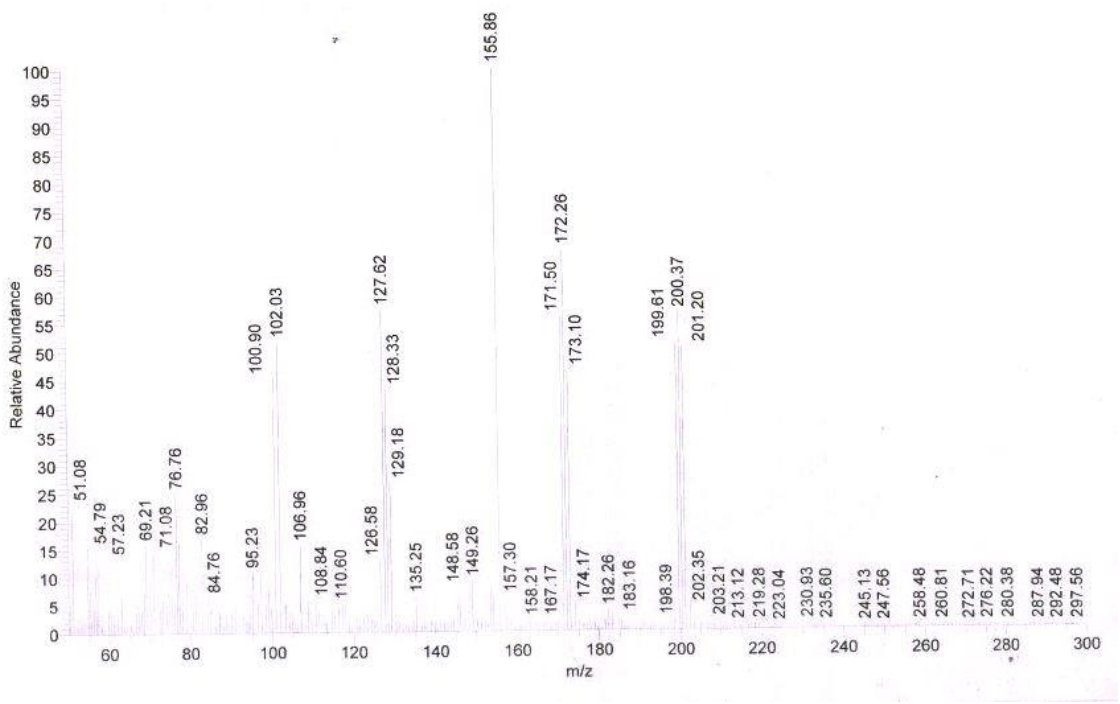

Fig. 5.14. Mass spectra of the product (2a).

(*E*)-Ethyl-2-cyano-3-(4-nitrophenyl) acrylate (2b)

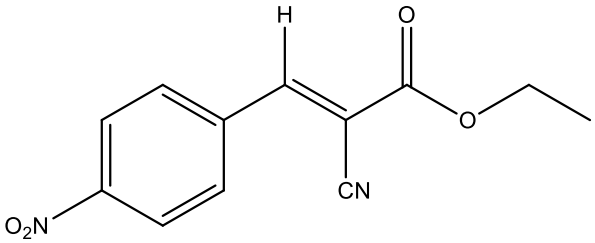

Yellow solid crystals (M.p. 157–159 °C). FTIR (KBr, cm^{-1}). 3096 (–C–H, stretch- ing, sp^2), 2993 (–C–H, stretching, sp^3), 2225 (–CN), 1720 (–C=O, ester), 1594, 1268 ($–NO_2$), 1415–1616 (–C=C, Ar), 1007 (–C=O, ester). ^{1}HNMR (400 MHz, $CDCl_3$) δ: 1.4 ($–CH_3$, t, J = 7.2 Hz, 3H), 4.4 (CH_2, q, J = 7.2 Hz, 2H), 8.1 (ArH, d, J = 8.8 Hz, 2H), 8.32–8.36 (Ar H, d, J = 8.8 Hz, 2H), 8.38 (–CH, s, 1H). ^{13}CNMR (400 MHz, $CDCl_3$) δ: 14.1 ($–CH_3$), 63.4 ($–O–CH_2$), 107.3 (–C–CN), 114.6 (–CN), 124.4, 131.5, 136.9, 149.7 ($–C–NO_2$), 151.8 (–C=C), 161.4 (–C=O). ESI–MS (m/z) = 246.08 $[M + H]^+$ (Figure 5.15 –5.18).

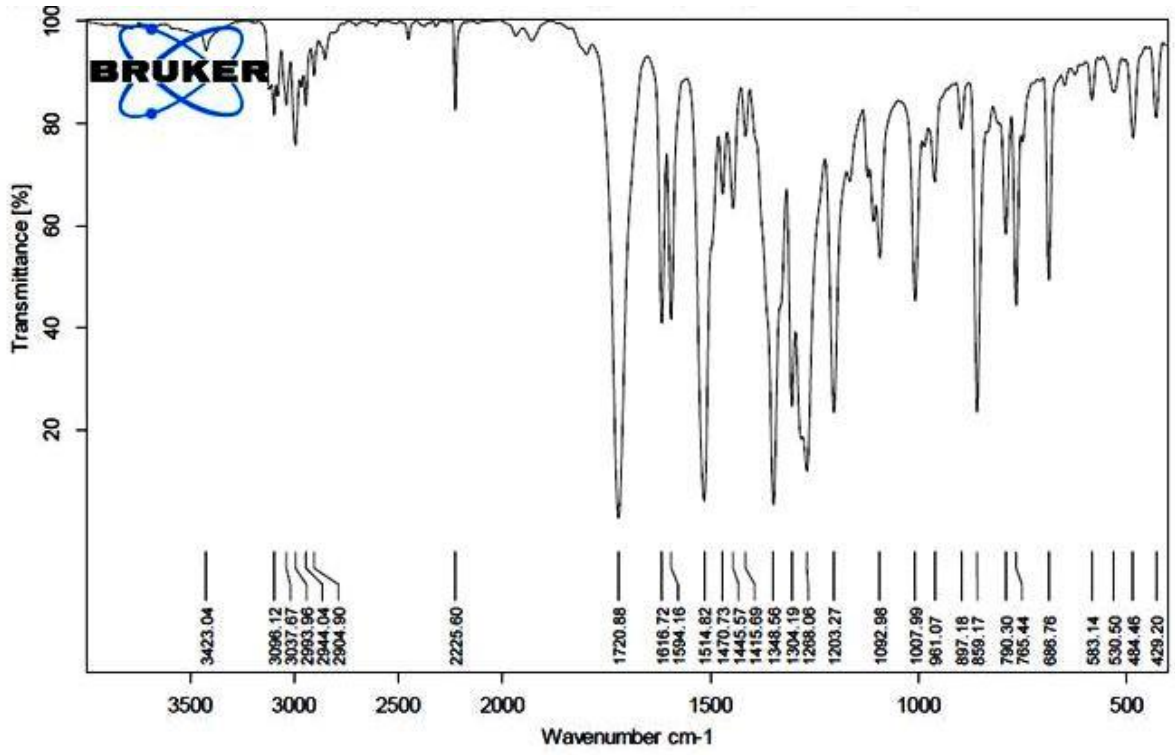

Fig. 5.15. FTIR spectra of the product (2b).

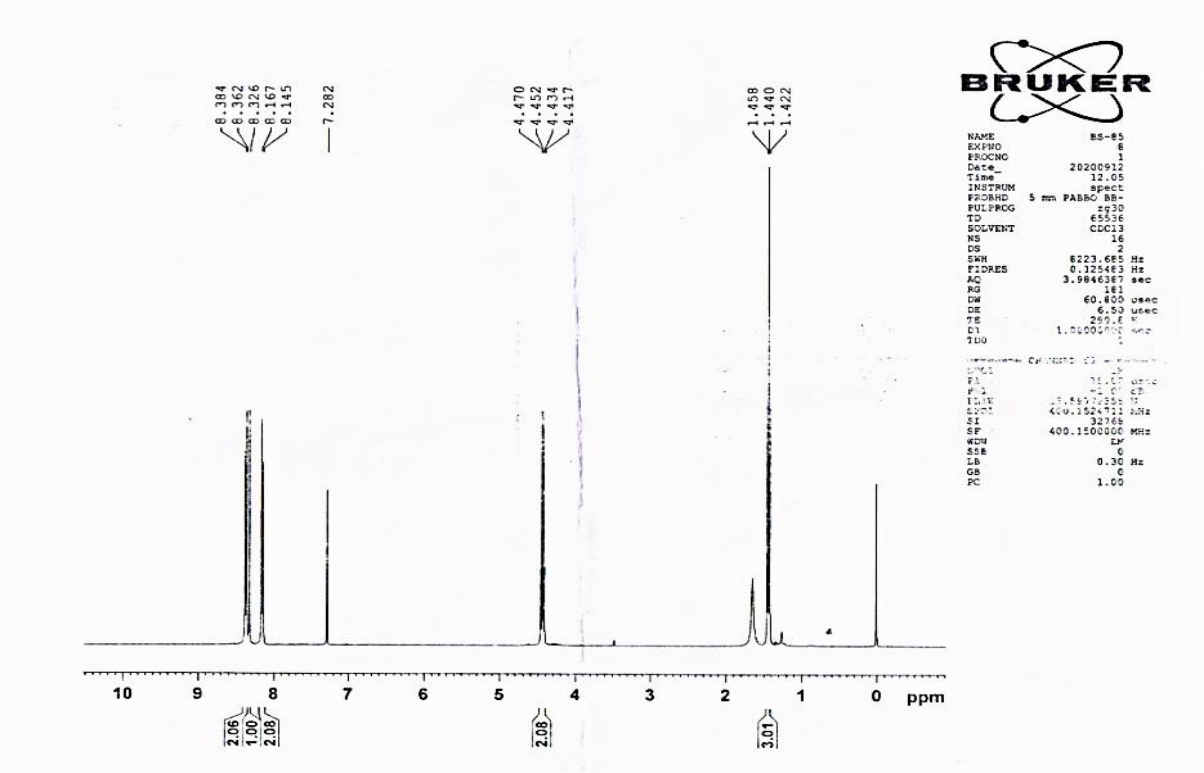

Fig. 5.16. ^{1}H-NMR spectra of the product (2b).

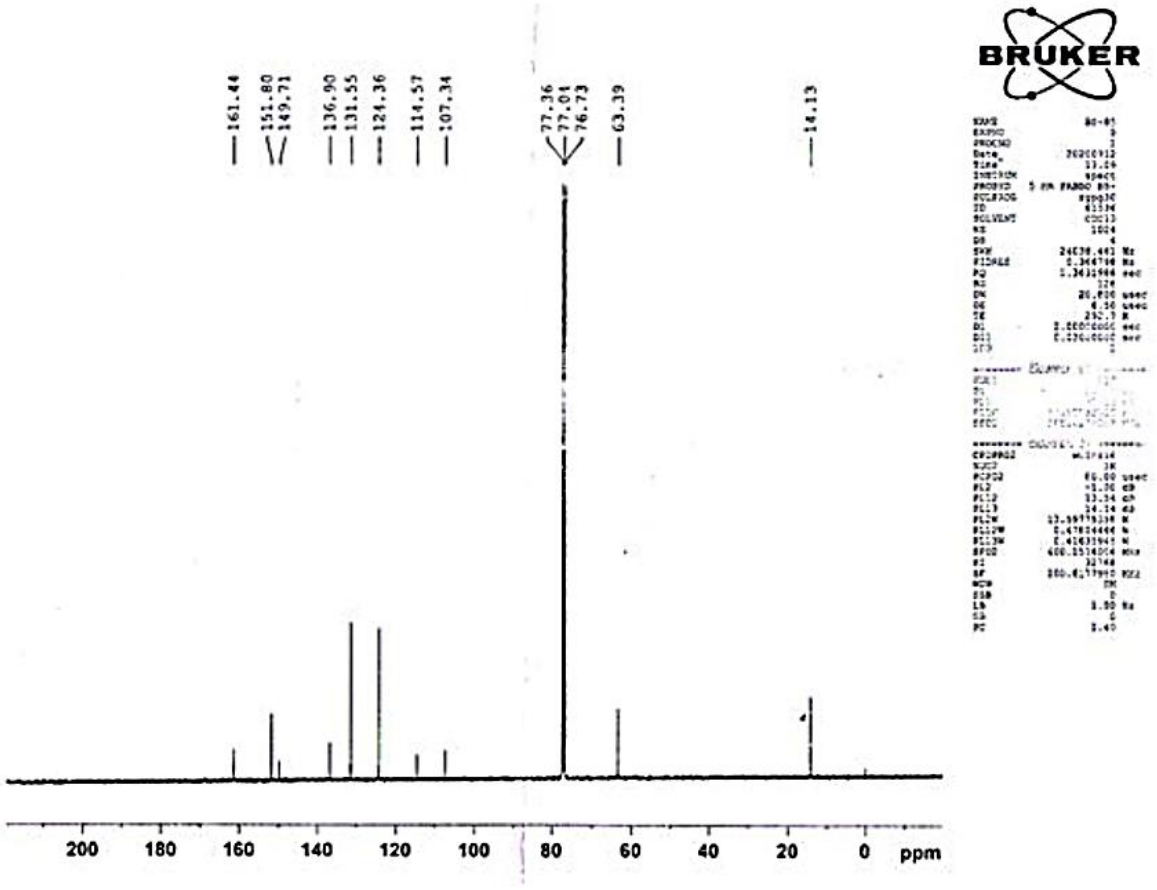

Fig. 5.17. ^{13}C-NMR spectra of the product (2b).

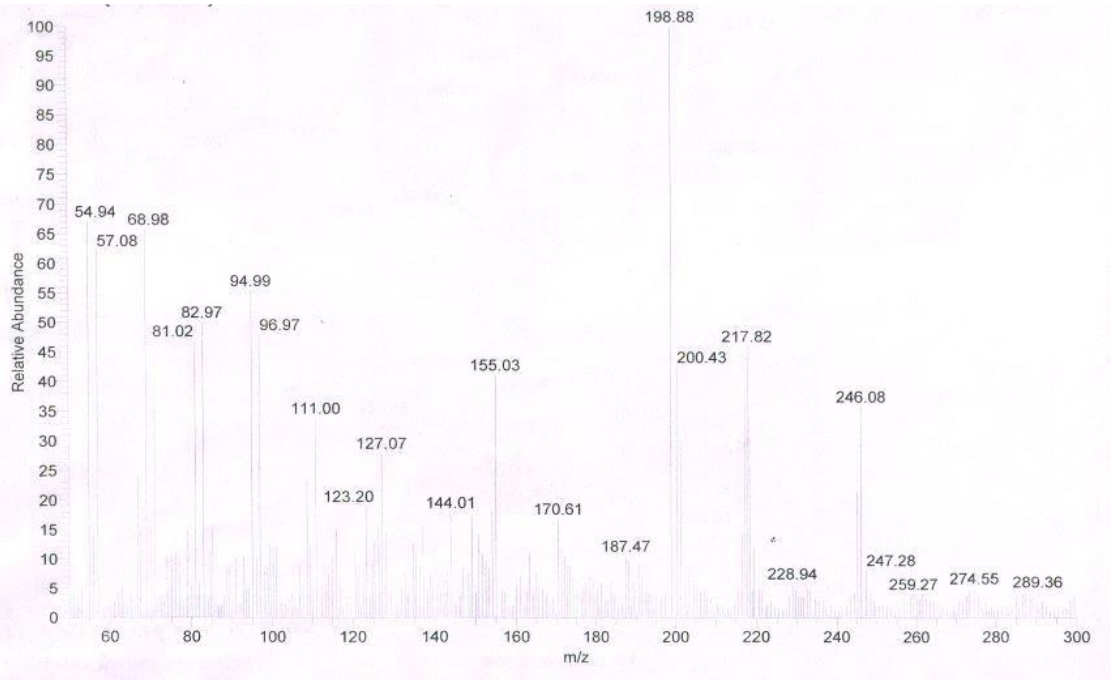

Fig. 5.18. Mass spectra of the product (2b).

(*E*)-Ethyl 2-cyano-3-(4-methoxyphenyl) acrylate (2c)

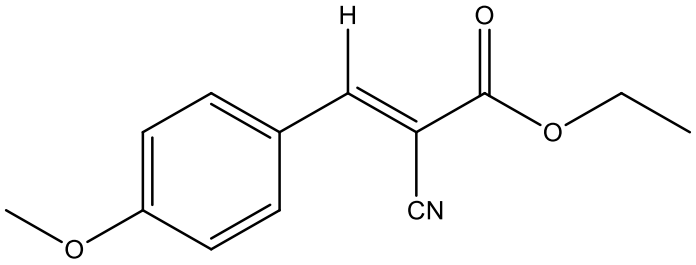

White solid crystals (M.p. 109–111 °C). FTIR (KBr, cm^{-1}). 1435, 1513, 1561 (–C=C, Ar), 1717 (–C=O), 2215 (–CN), 2843, 2992 (–CH, str), 3025 (–CH, str). ^{1}HNMR (400 MHz, $CDCl_3$) δ: 1.42 (–CH_3, t, J = 7.2 Hz, 3H), 3.90 (–O–CH_3, s, 3H), 4.40 (–CH_2, q, J = 7.0 Hz, 2H), 6.99–7.01 (Ar H, d, J = 8.8 Hz, 2H), 8.0 (ArH, d, J = 8.8 Hz, 2H), 8.2 (=CH, s, 1H). ^{13}CNMR (400 MHz, $CDCl_3$) δ: 14.2 (–CH_3), 55.6(–OCH_3), 62.5 (–OCH_2), 99.3 (–C–CN), 116.3 (–CN), 114.8, 124.3, 133.7, 154.5, 163.2, 163.8 (–C=O). ESI–MS (m/z) = 231.28 [M + H]$^{+}$ (Figure 5.19–5.22).

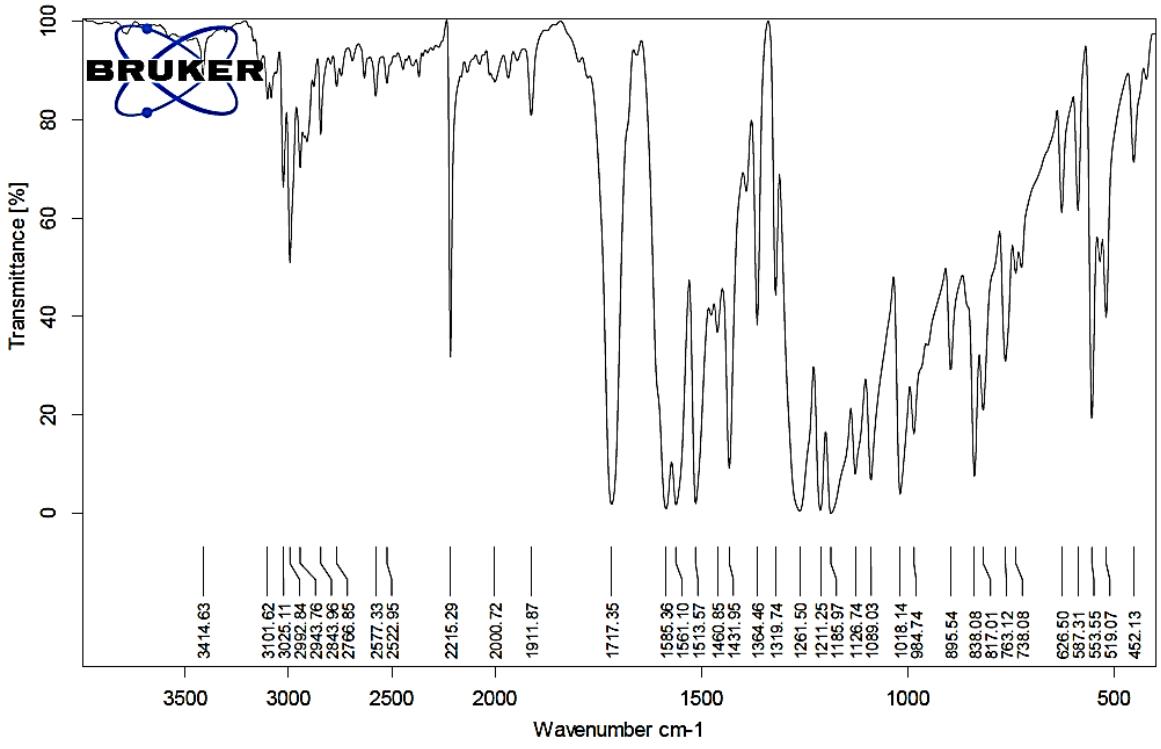

Fig. 5.19. FTIR spectra of the product (2c).

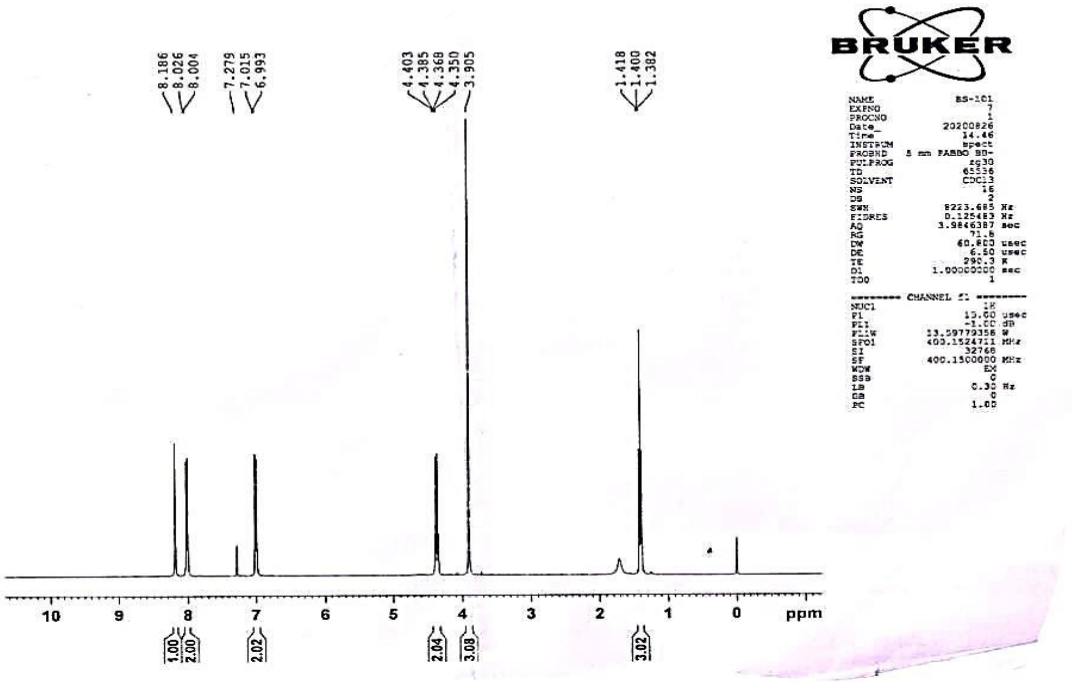

Fig. 5.20. ^{1}H-NMR spectra of the product (2c).

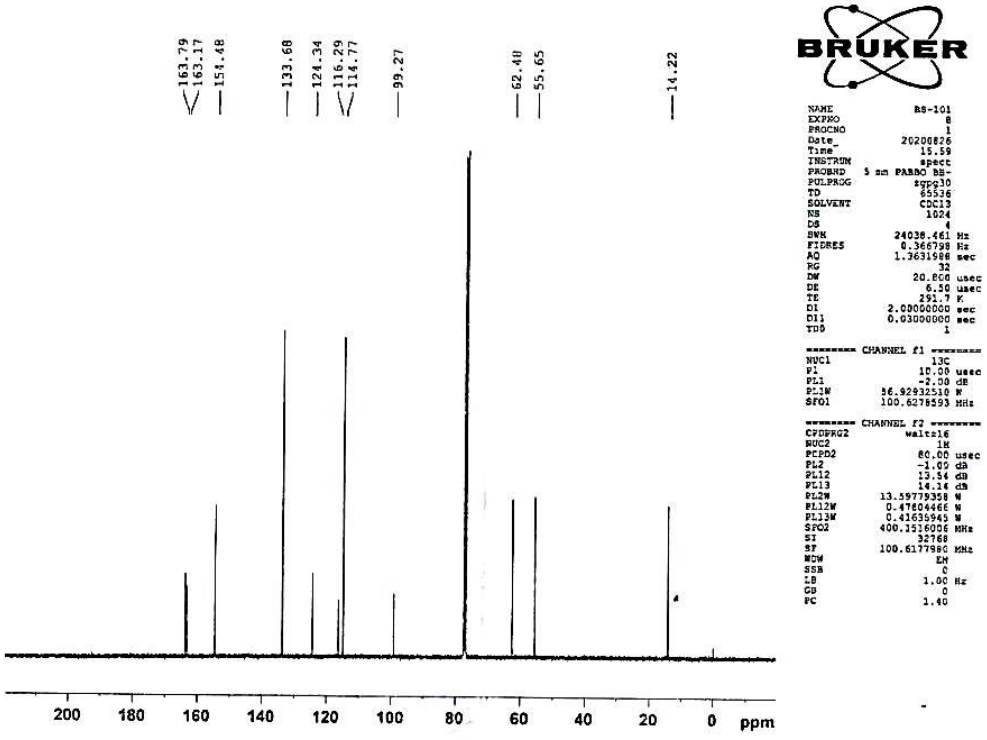

Fig. 5.21. ^{13}C-NMR spectra of the product (2c).

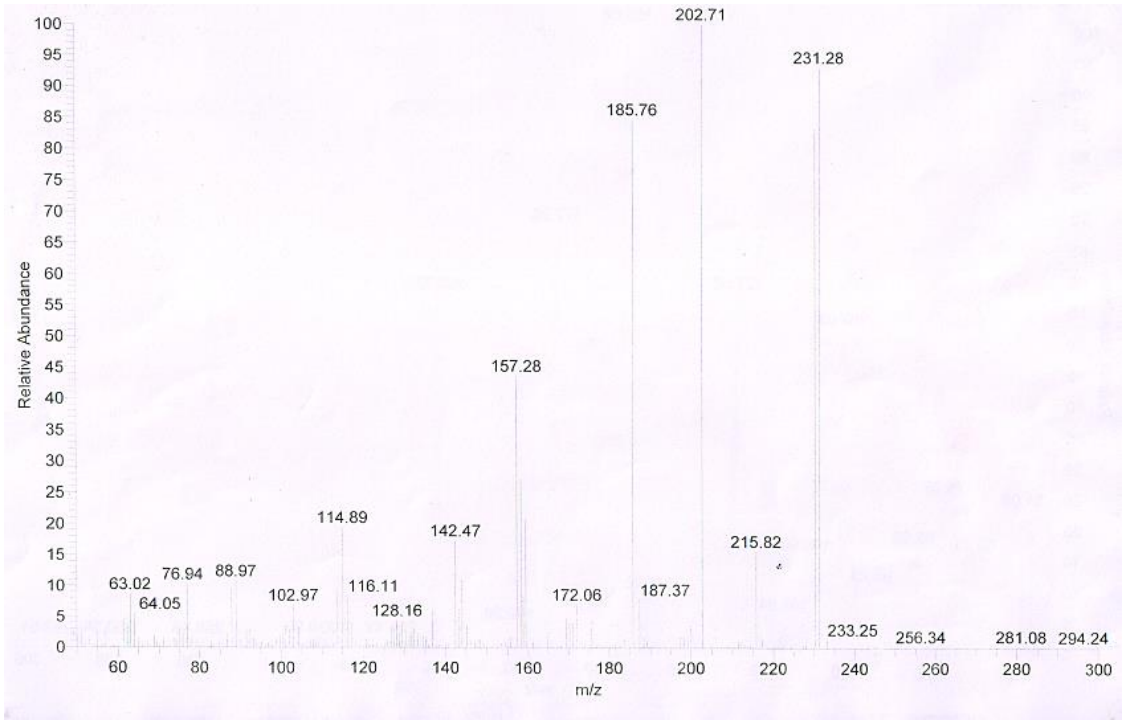

Fig. 5.22. Mass spectra of the product (2c).

(*E*)-Ethyl-2-cyano-3-(p-tolyl) acrylate (2d)

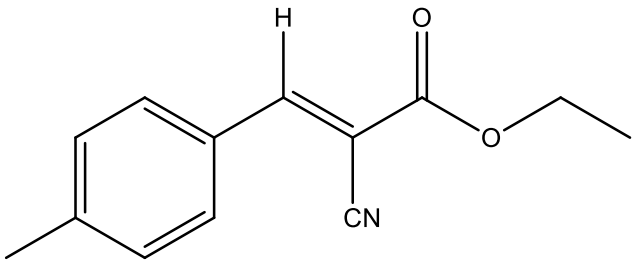

White solid crystals (m.p. 110–113 °C). FTIR (KBr, cm^{-1}). 3029 (–C–H, *stretching*, sp^2), 2993 (–C–H, stretching, sp^3), 2216 (–CN), 1724 (–C=O, ester), 1420–1596 (–C=C–Ar), 1093 (–C–O, ester). ^{1}HNMR (400 MHz, $CDCl_3$) δ: 1.42 (CH_3, t, J = 7.2 Hz, 3H), 2.44 (CH_3, s, 3H), 4.41 (CH_2, q, J = 6.8 Hz, 2H), 7.6 (ArH, d, J = 8.8 Hz, 2H), 7.8 (Ar H, d, J = 8.4 Hz, 2H), 8.2 (=CH, s, 1H). ^{13}CNMR (400 MHz, $CDCl_3$) δ: 14.2 (–CH_3), 21.9 (Ar– CH_3), 62.6 (O–CH_2), 101.5 (–C–CN), 115.8 (–CN), 128.8, 130.0, 131.2, 144.7, 162.8 (–C=O), 155.0 (–C=C). ESI–MS (m/z) = 215.19 $[M + H]^+$ (Figure 5.23 –5.26).

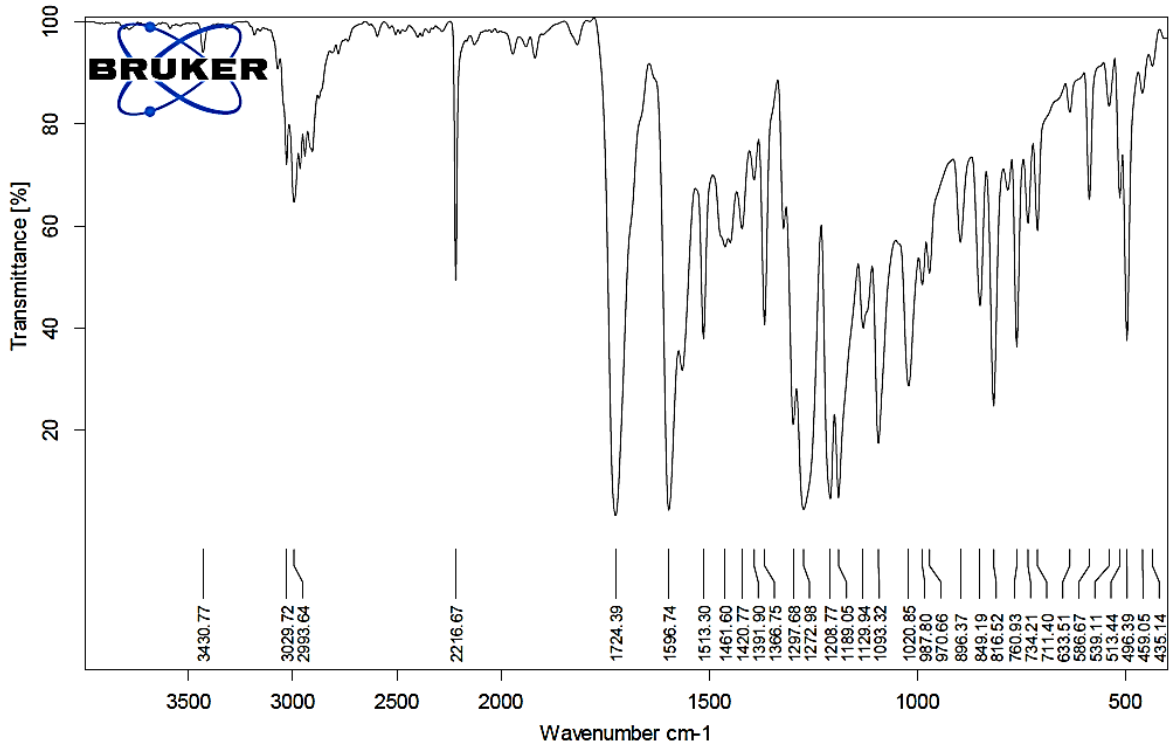

Fig. 5.23. FTIR spectra of the product (2d).

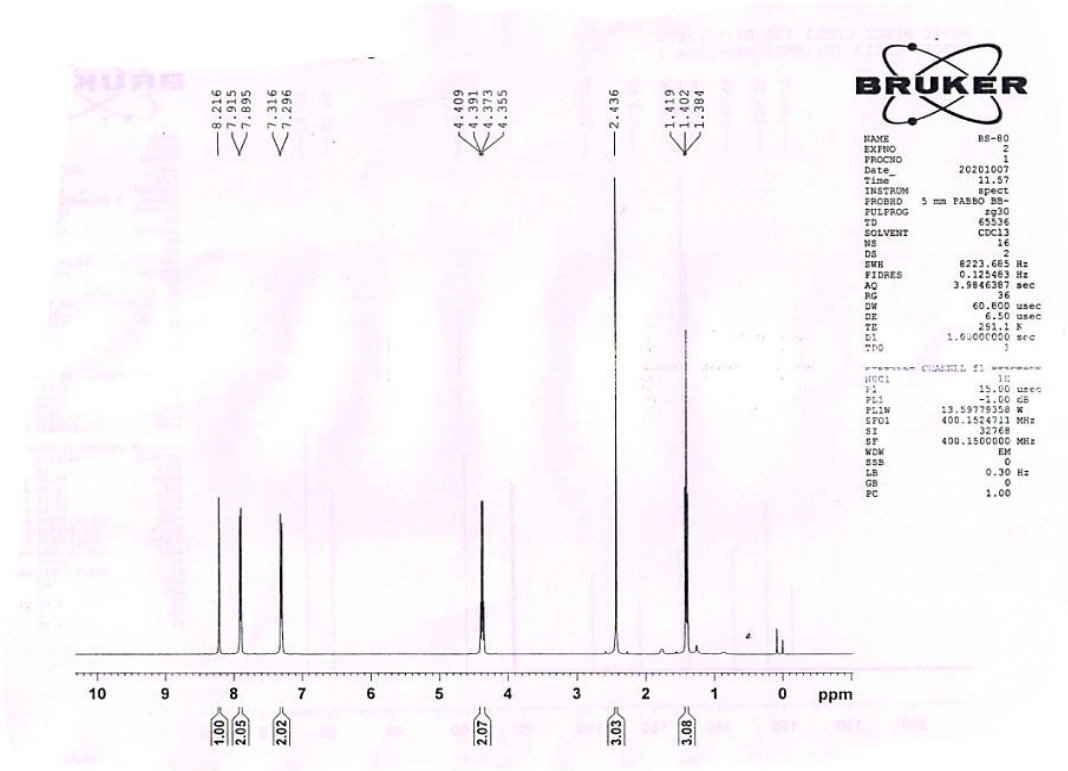

Fig. 5.24. ^{1}H NMR spectra of the product (2d).

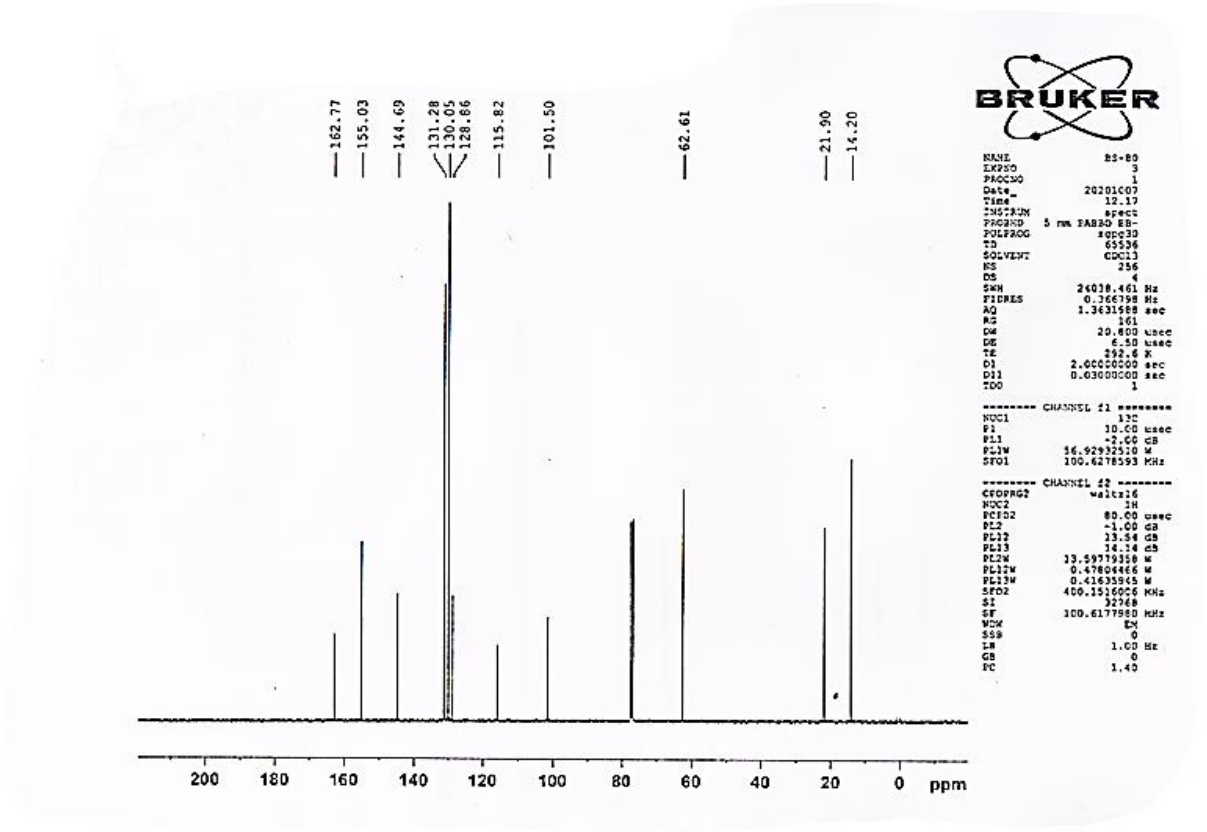

Fig. 5.25. ^{13}C-NMR spectra of the product (2d).

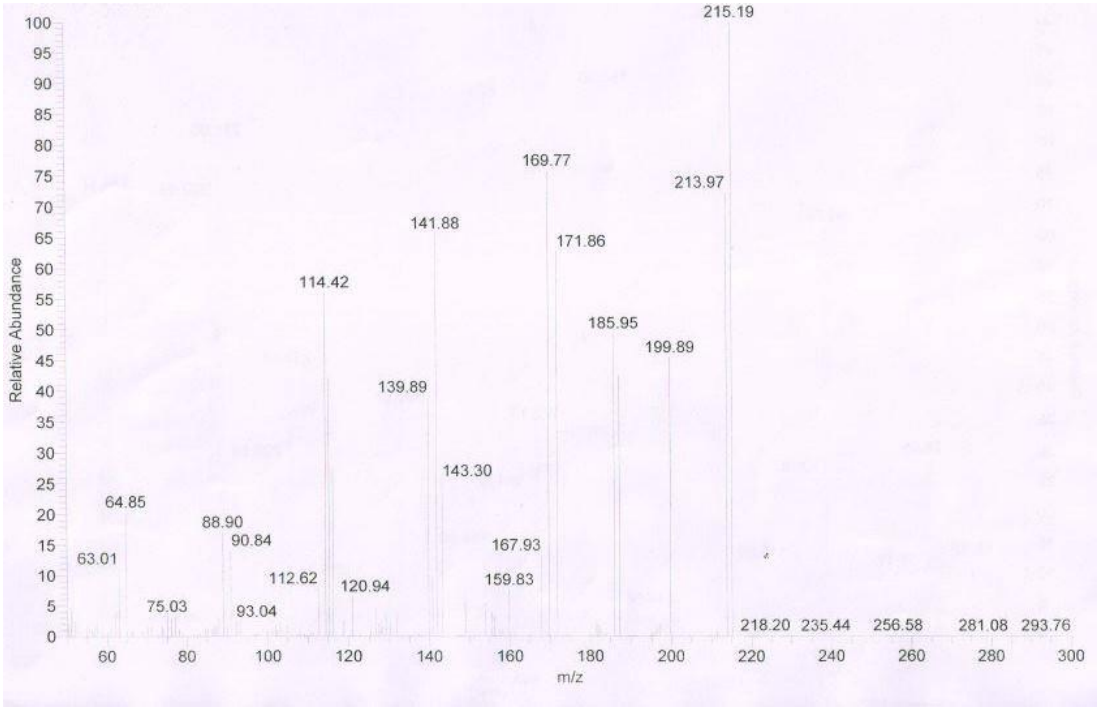

Fig. 5.26. Mass spectra of the product (2d).

(*E*)-Ethyl-2-cyano-3-(4-chlorophenyl) acrylate (2e)

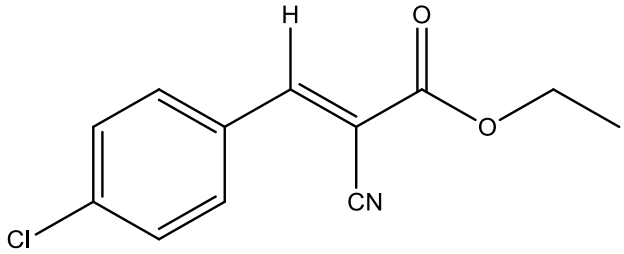

White solid crystals (M. p. 159–160 °C). FTIR (KBr, cm^{-1}). 3431 (–C–H, stretching, sp^2), 2954 (–C–H, stretching, sp^3), 2223 (–CN), 1726 (–C=O, ester), 1411–1611 (–C=C, Ar), 1206 (–C–O, ester), 1081 (Ar–Cl). ^{1}HNMR (400 MHz, $CDCl_3$) δ: 1.43 (–CH_3, t, J = 7.2 Hz, 3H), 4.43 (–CH_2, q, J = 7.2 Hz, 2H), 7.48 (Ar H, d, J = 6.8 Hz, 2H) 7.93–7.96 (Ar H, d, J = 6.8 Hz, 2H), 8.22 (= CH, s, 1H). ^{13}CNMR (400 MHz, $CDCl_3$) δ: 14.2 (–CH_3), 62.9 (–O–CH_2), 103.4 (–C–CN), 115.3 (–CN), 129.7, 132.2, 139.6, 153.5, 162.3 (–C=O). ESI–MS (m/z) = 235.09 $[M + H]^+$ (Figure 5.27 –5.30).

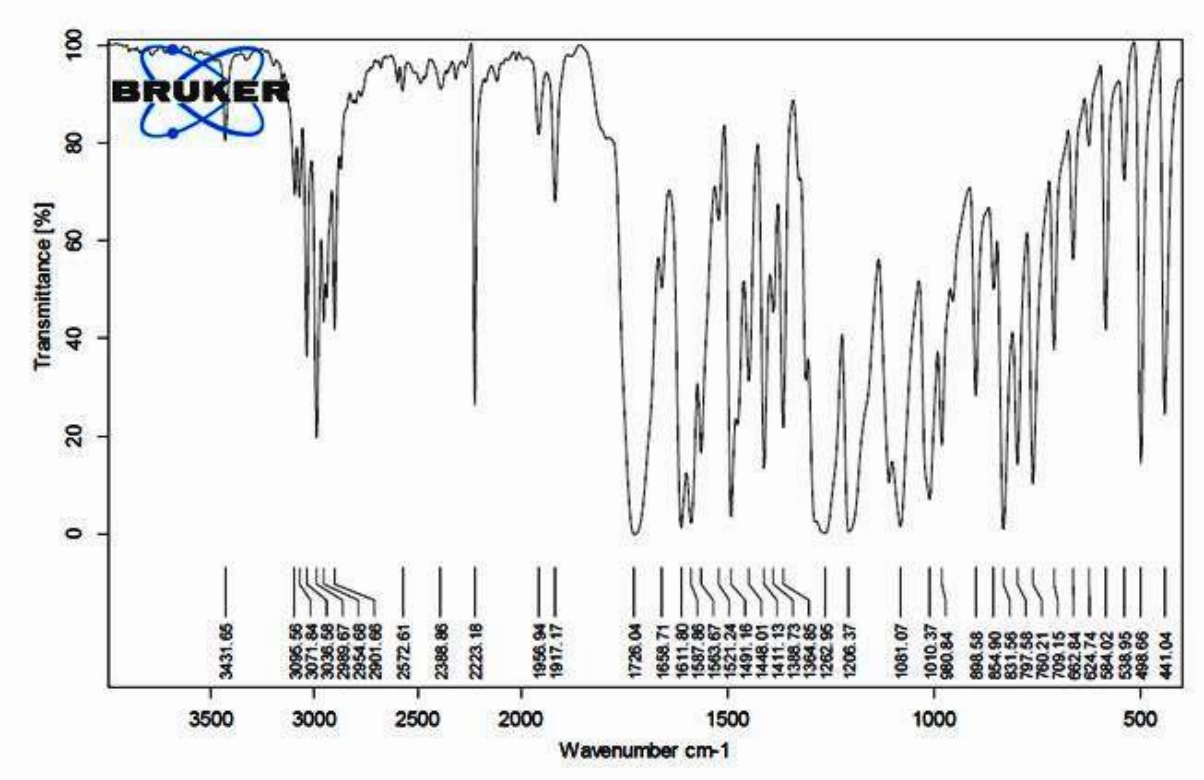

Fig. 5.27. FTIR spectra of the product (2e).

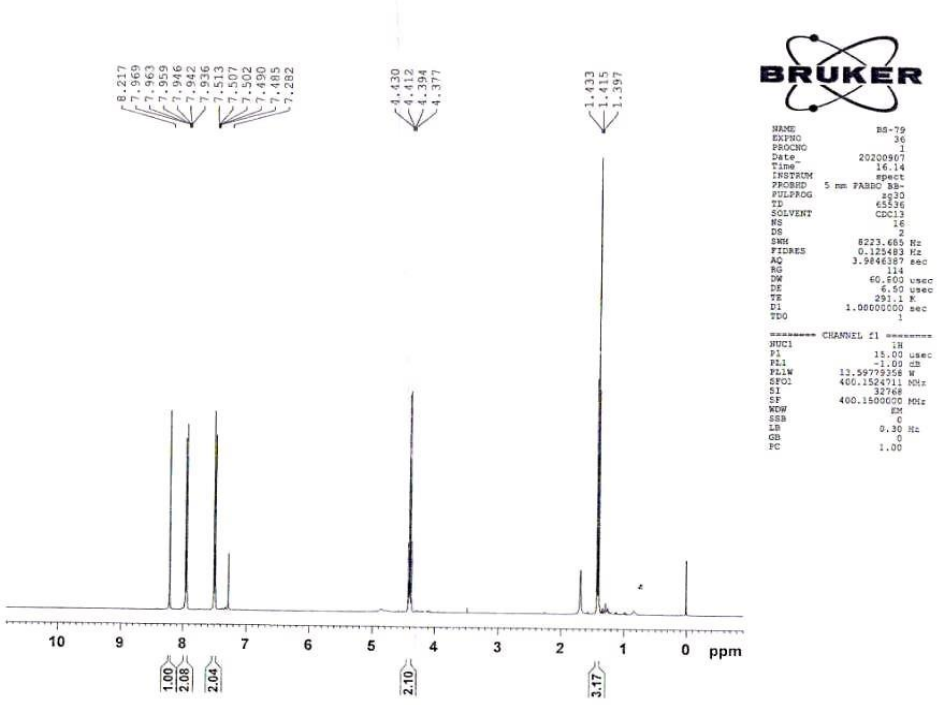

Fig. 5.28. ^{1}H-NMR spectra of the product (2e).

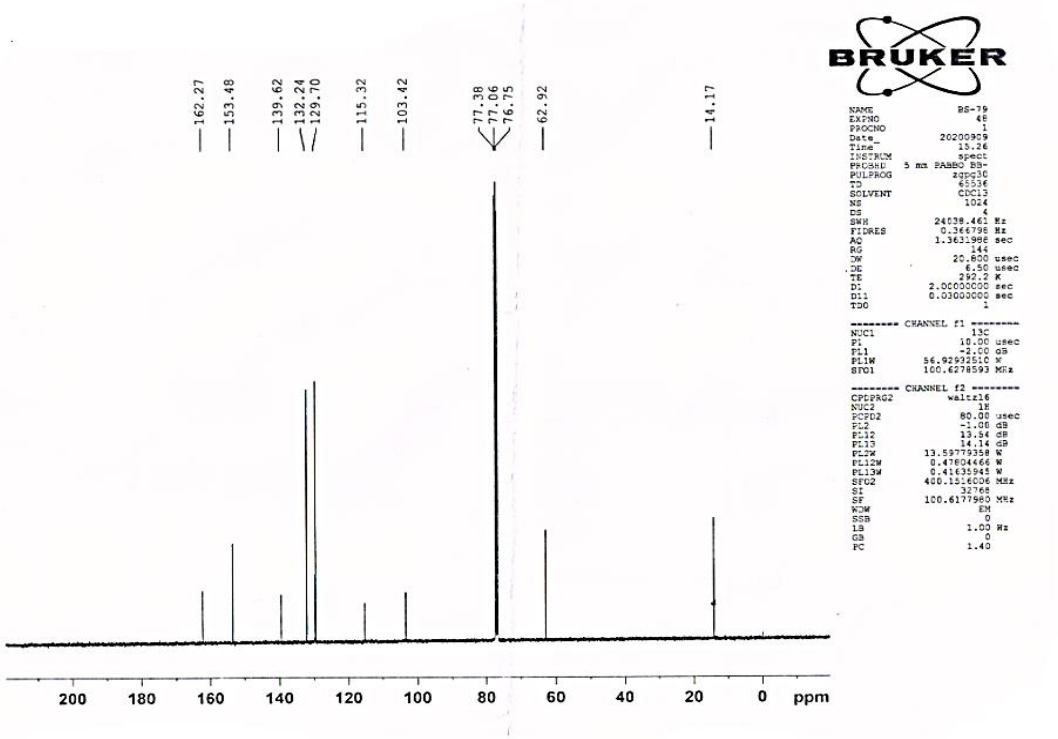

Fig. 5.29. ^{13}C-NMR spectra of the product (2e).

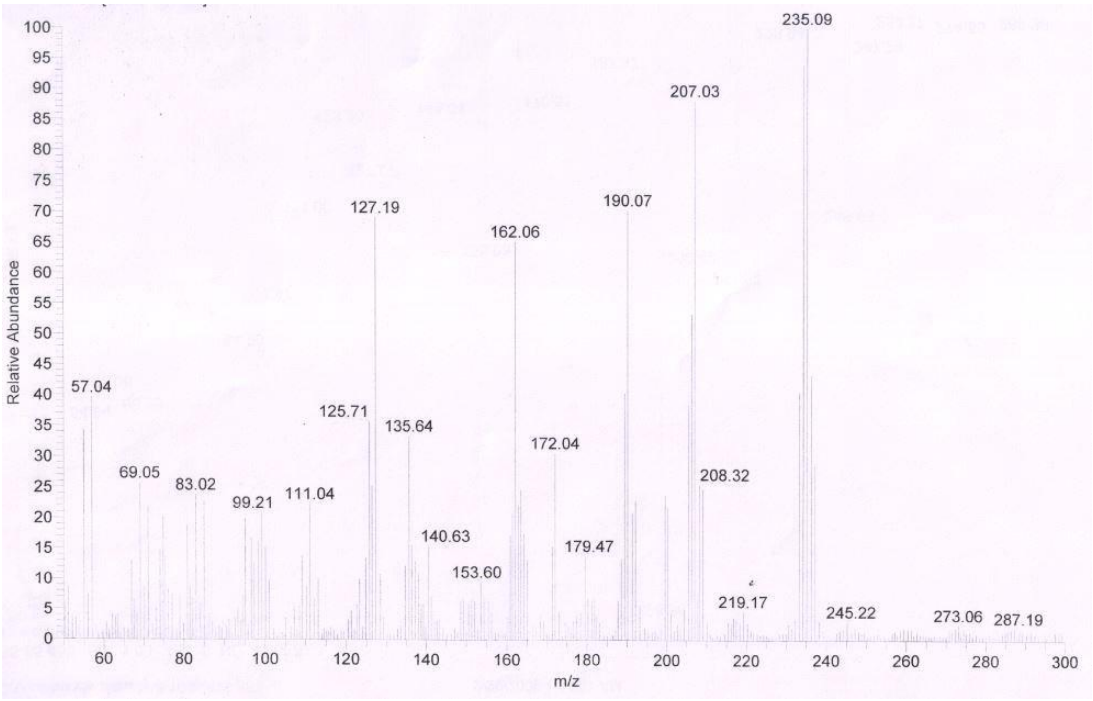

Fig. 5.30. Mass spectra of the product (2e).

(*E*)-Ethyl-2-cyano-3-(4-bromophenyl) acrylate (2f)

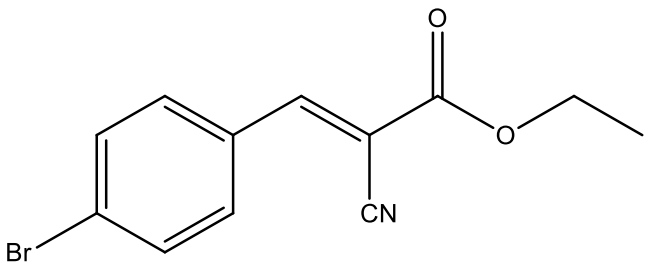

White solid crystals (M. p. 80 –82 °C). FTIR (KBr, cm^{-1}) 3430 (–C–H, stretching, sp^2) 2952 (–C–H, stretching, sp^3), 2222 (–CN), 1725 (–C=O, ester), 1487–1611 (Ar, C=C), 1205 (–C–O, ester), 1094 (Ar–Br). ^{1}H NMR (400 MHz, $CDCl_3$) δ: 1.4 (CH_3, t, J = 7.2 Hz, 3H), 4.4 (CH_2, q, J = 6.8 Hz, 2H), 7.6 (Ar H, d, J = 8.8 Hz, 2H), 7.8 (ArH, d, J = 8.4 Hz, 2H), 8.2 (=CH, s, 1H). ^{13}C NMR (400 MHz, $CDCl_3$) δ:14.2 (–CH_3), 62.9 (–O–CH_2), 103.6 (–C–CN), 115.3 (–CN), 128.3, 130.2, 132.2, 132.7, 153.6 (–C=C), 162.2 (–C=O). ESI–MS (m/z) = 280.06 $[M + H]^+$ (Figure 5.31–5.34).

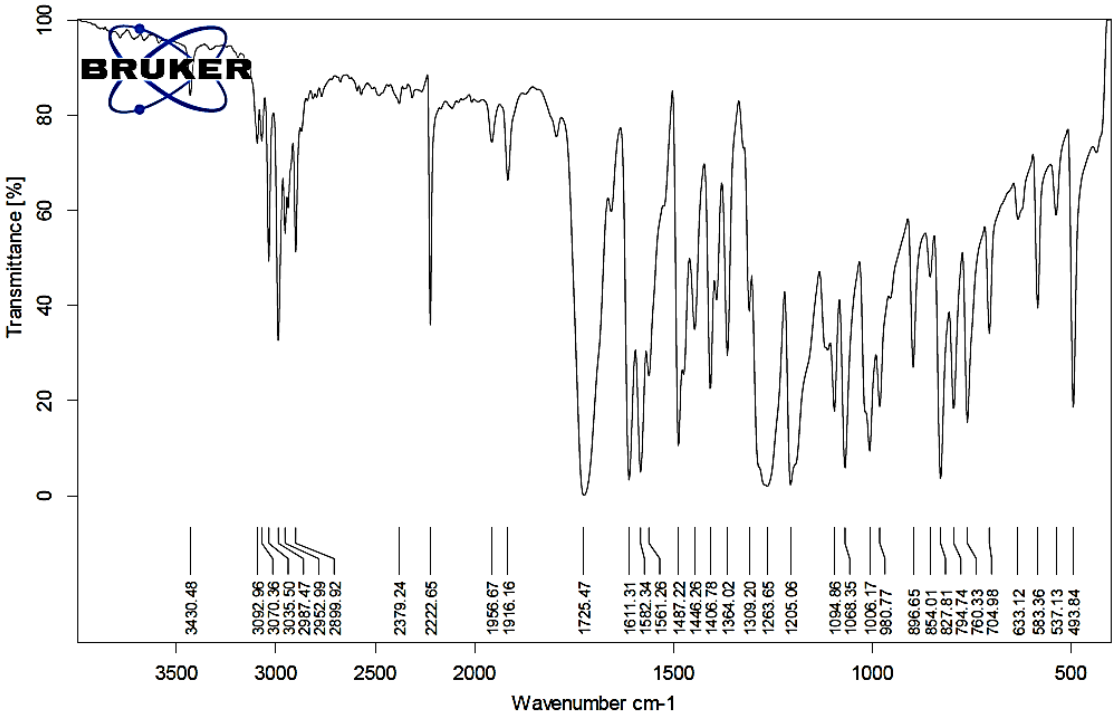

Fig. 5.31. FTIR spectra of the product (2f).

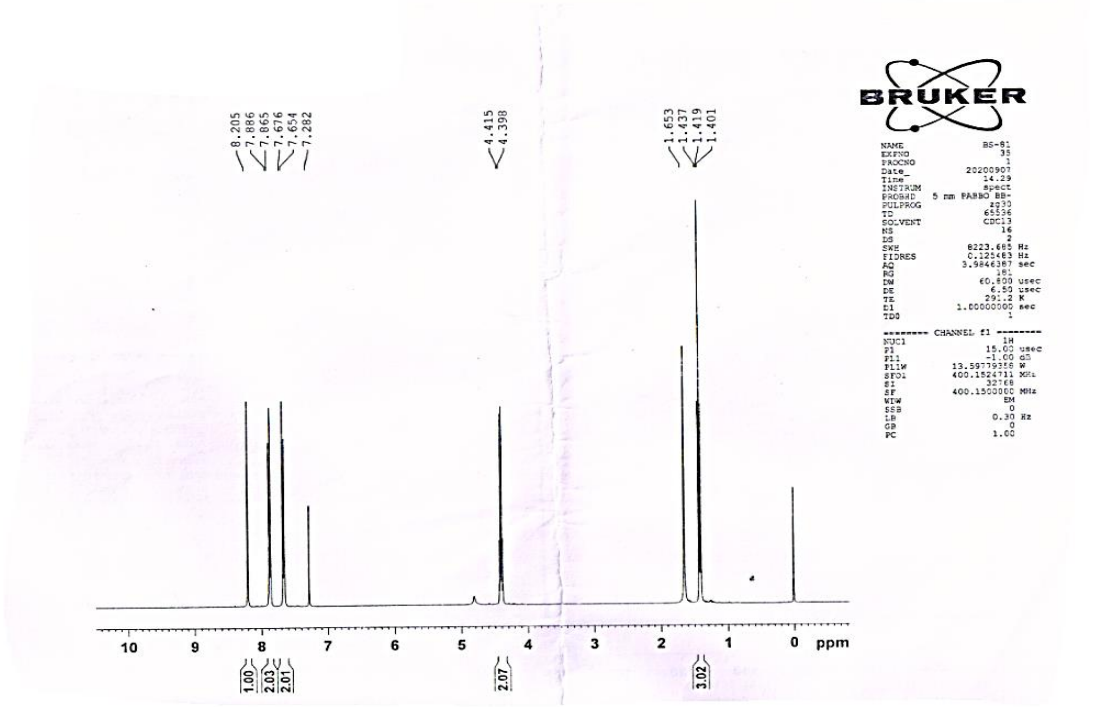

Fig. 5.32. ^{1}H-NMR spectra of the product (2f).

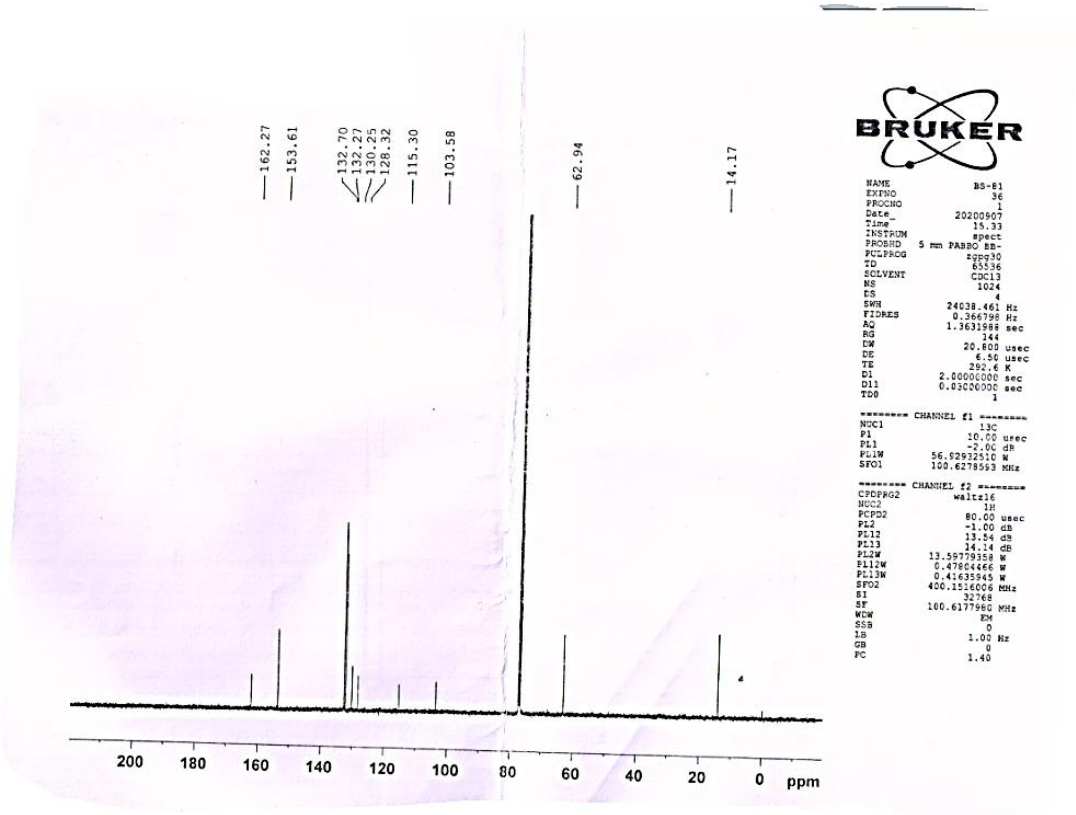

Fig. 5.33. ^{13}C-NMR spectra of the product (2f).

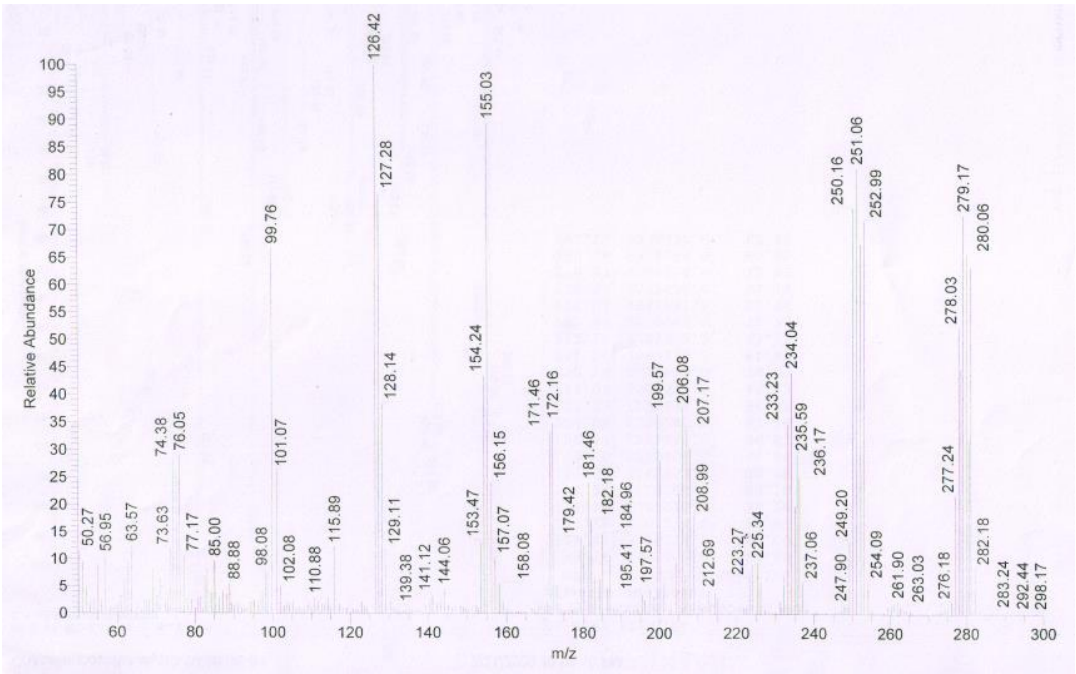

Fig. 5.34. Mass spectra of the product (2f).

(*E*)-Ethyl-2-cyano-3-(2-bromophenyl) acrylate (2 g)

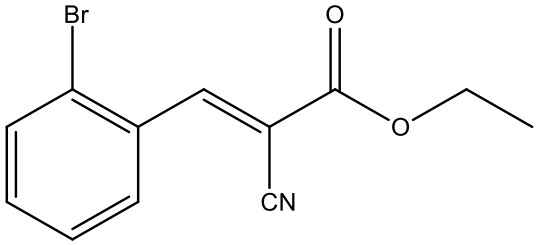

White solid crystals (M. p. 81–83 °C). FTIR (KBr, cm^{-1}) 3430 (–C–H, stretching, sp^2) 2952 (–C– H, stretching, sp^3), 2222 (–CN), 1725 (–C=O, ester), 1487–1611 (Ar, C=C), 1205 (–C–O, ester), 1094 (Ar–Br). ^{1}H NMR (400 MHz, $CDCl_3$) δ: 1.4 (CH_3, t, J = 7.2 Hz, 3H), 4.4 (CH_2, q, J = 6.4 Hz, 2H), 7.2 (Ar H, t, J = 7.6 Hz, 1H), 7.3 (Ar H, t, J = 7.6 Hz, 1H), 7.5 (Ar H, d, J = 8.0 Hz, 1H), 8.0 (ArH, d, J = 7.6 Hz, 1H), 8.6 (=CH, s, 1H). ^{13}C NMR (400 MHz, $CDCl_3$) δ: 14.2 (–CH_3), 63.0 (O–CH_2), 106.4 (C–CN), 114.7 (–CN), 126.6, 128.1, 130.1, 131.7, 133.6, 133.7, 153.9 (–C=C), 161.8 (–C=O). ESI–MS (m/z) = 280.06 $[M + H]^+$ (Figure 5.35–5.38).

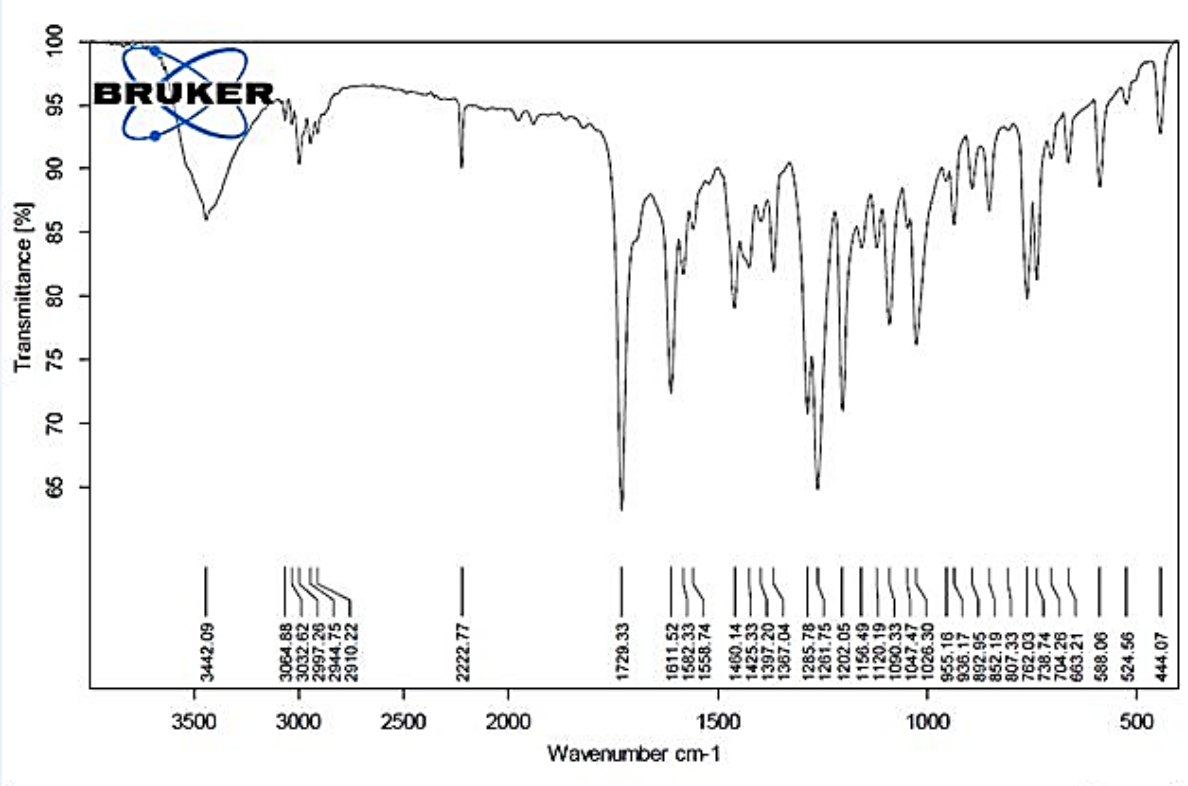

Fig. 5.35. FTIR spectra of the product (2g).

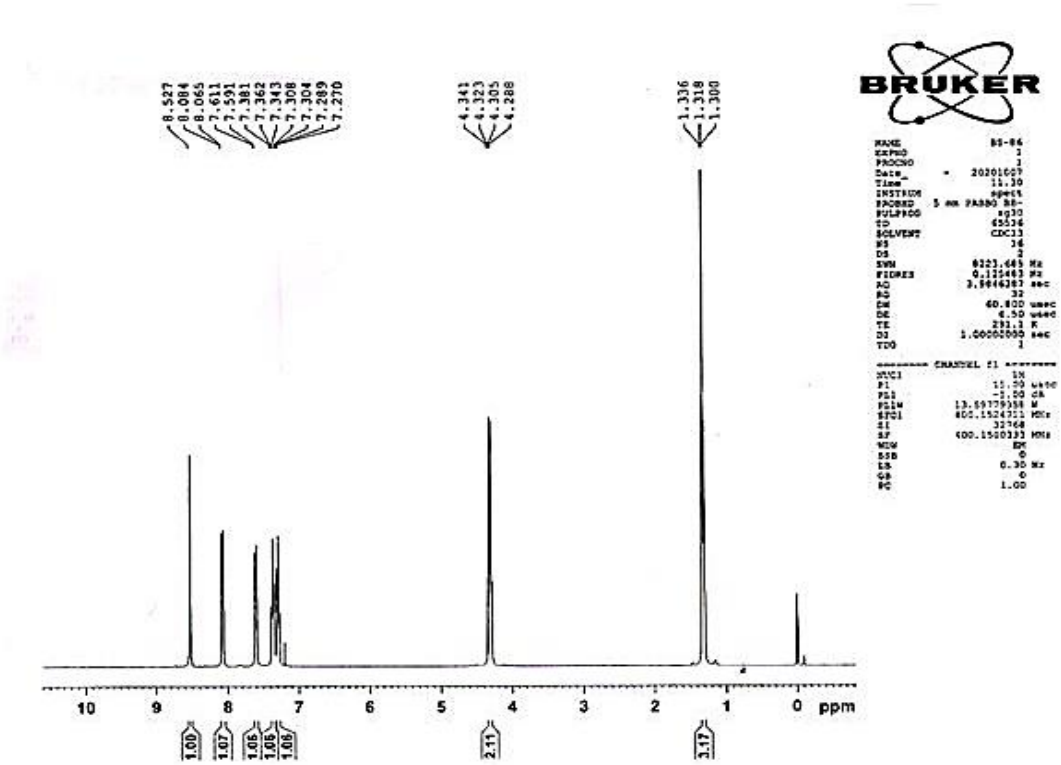

Fig. 5.36. ^{1}H-NMR spectra of the product (2g).

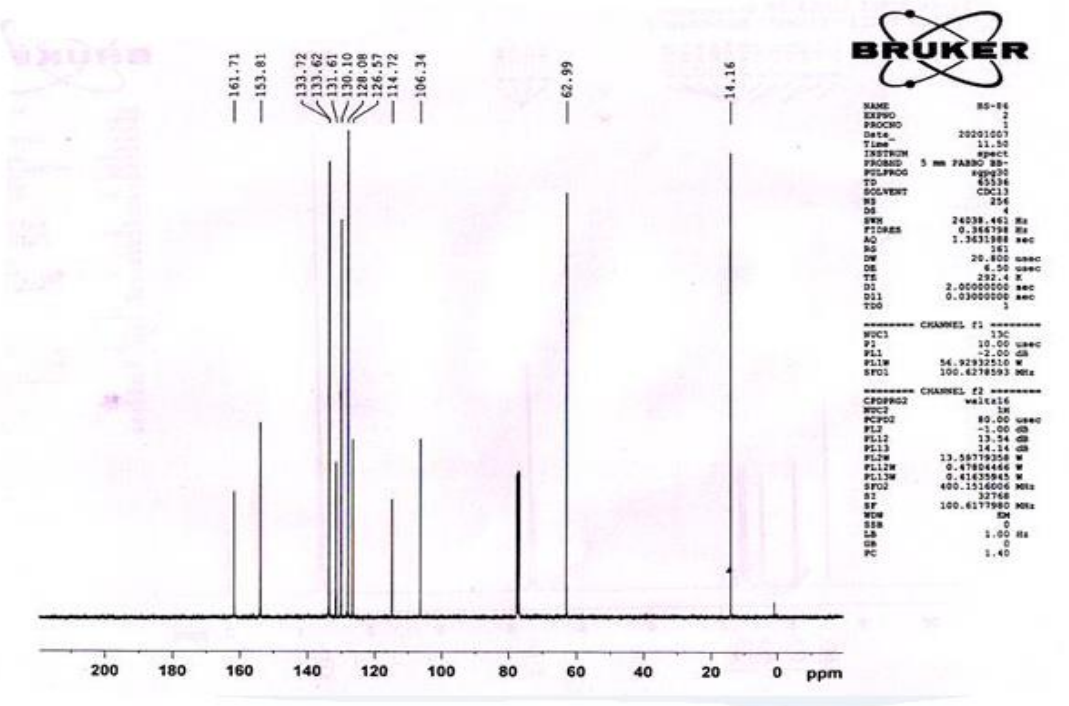

Fig. 5.37. ^{13}C-NMR spectra of the product (2g).

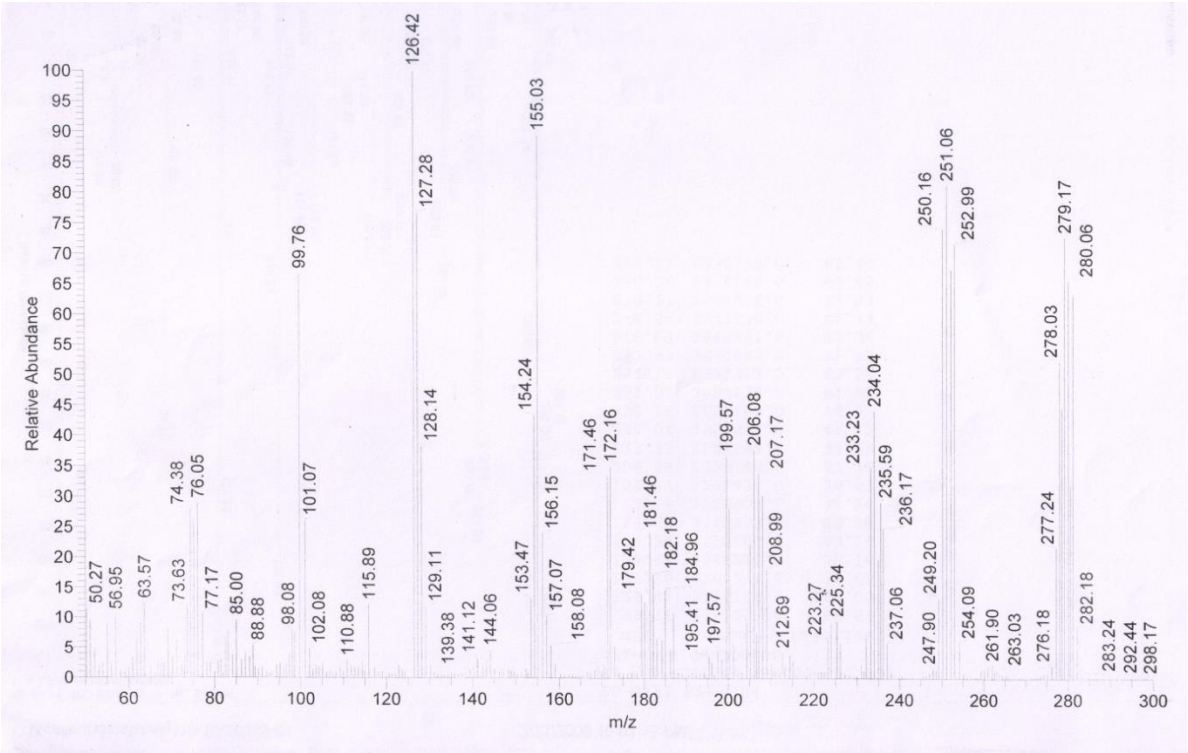

Fig. 5.38. Mass spectra of the product (2g).

Ethyl-2-cyano-4-nitro-3-phenyl butanoate (3a)

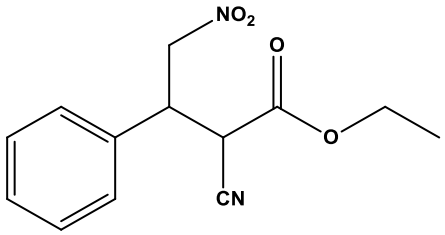

Colorless oil. ^{1}H NMR (400 MHz, $CDCl_3$). δ: 7.41 (m, J = 7.6 Hz, 10 H), 5.05 (m, J = 6.8 Hz, 4H), 4.27 (m, J = 7.6 Hz, 6H), 3.95 (m, J = 5.6 Hz, 2H), 1.17 (t, J = 7.2 Hz, 6H). ^{13}C NMR (400 MHz, $CDCl_3$) δ: 13.8 (–CH_3), 41.5 (–C–CH_2), 43.1 (–C–CN), 63.7 (–OCH_2–), 76.3 (–CH_2–NO_2), 114.4 (–CN), 127.5, 129.3, 129.5, 134.5 (–C=C), 163.9 (–C=O) (Figure 5.39 –5.40).

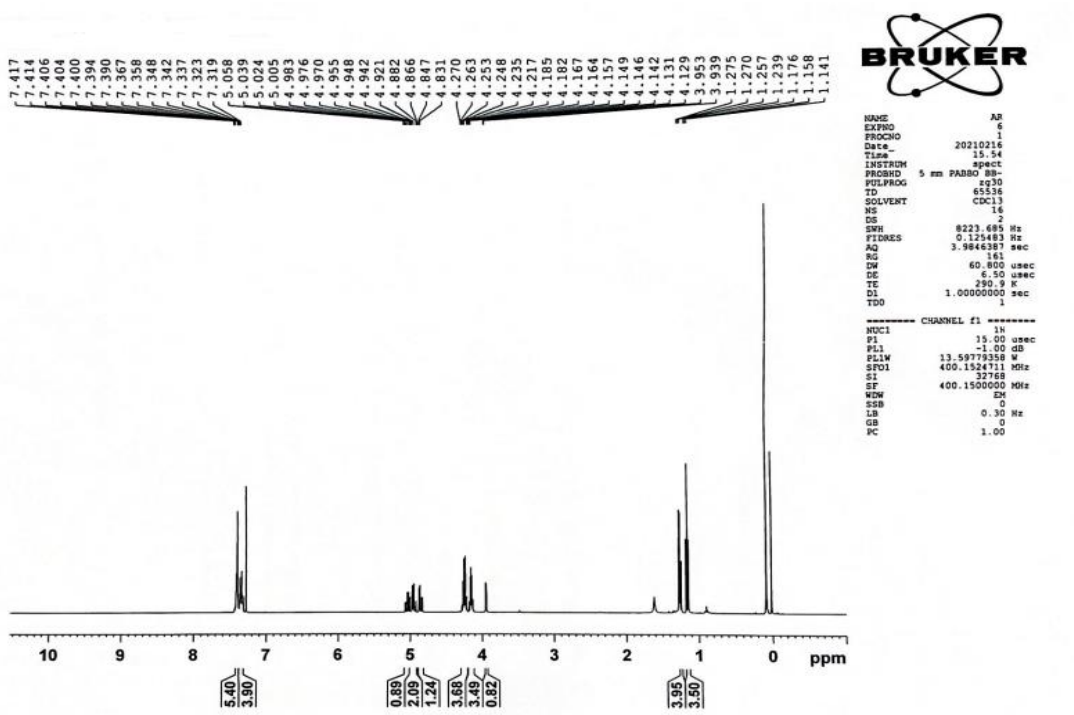

Fig. 5.39. ^{1}H-NMR spectra of product (3a).

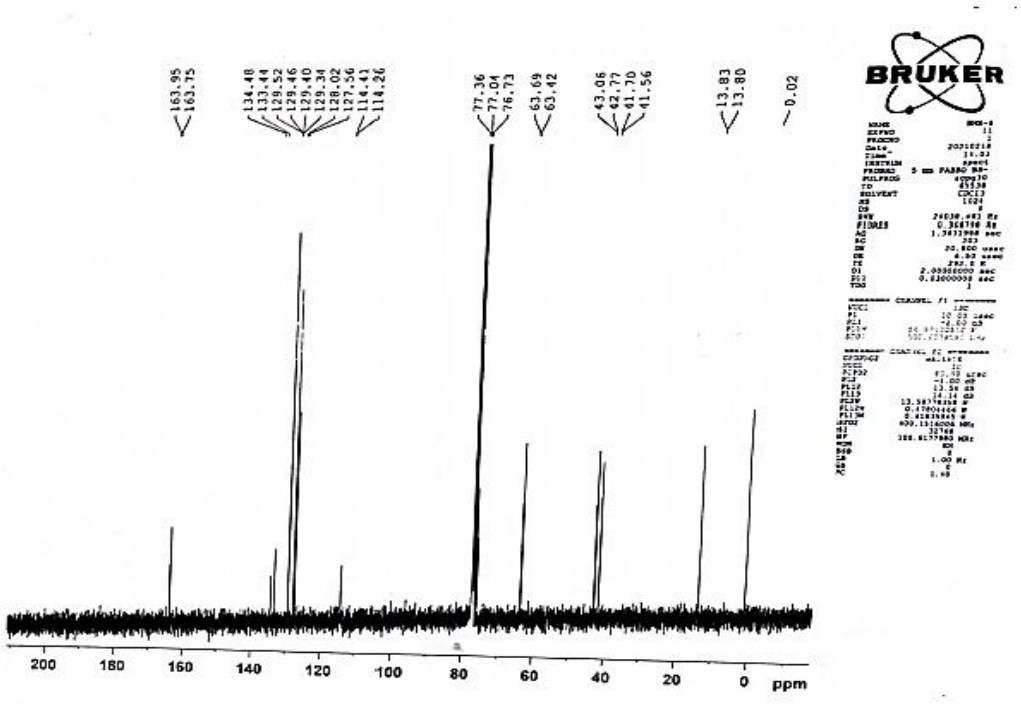

Fig. 5.40. ^{13}C-NMR spectra of product (3a).

Ethyl 2-cyano-4-nitro-3-(4-nitrophenyl) butanoate (3b)

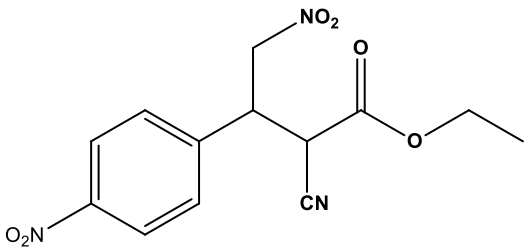

Colorless oil.[1]H NMR (400 MHz, $CDCl_3$) δ: 8.27 (m, J = 6.8 Hz, 4H), 7.5 (m, J = 8.0 Hz, 4H), 5.06 (m, J = 7.6 Hz, 4H), 4.43 (m, J = 5.6 Hz, 6H), 4.02 (m, J = 6.8 Hz, 2H), 1.28 (t, J = 7.2 Hz, 3H) (Figure 5.41).

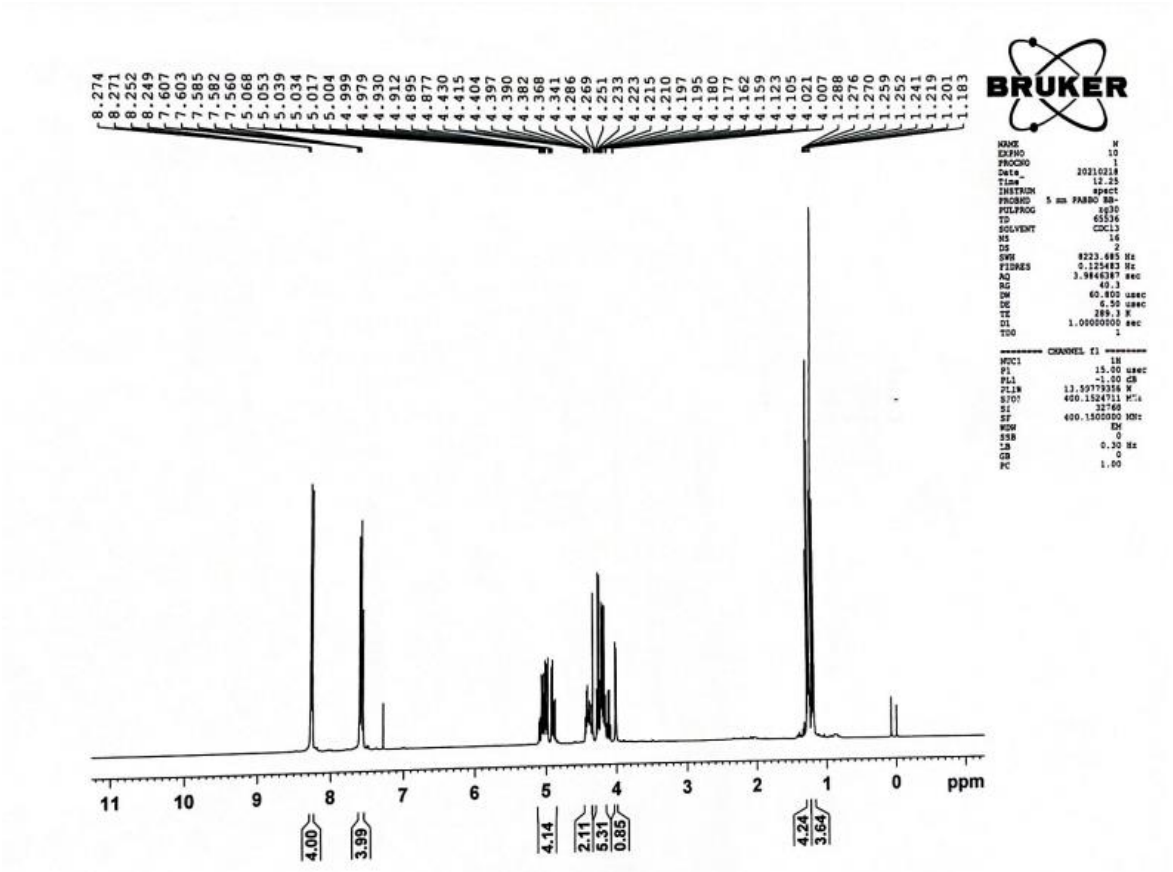

Fig. 5.41. [1]H-NMR spectra of the product (3b).

Ethyl 2-cyano-4-nitro-3-(4-methoxy phenyl) butanoate (3c)

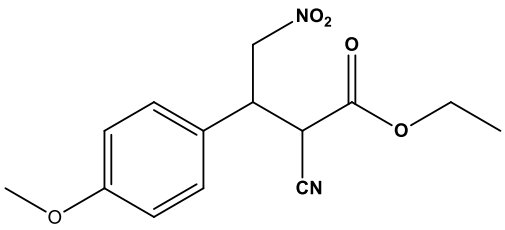

Colorless oil. ^{1}H NMR (400 MHz, $CDCl_3$) δ: 7.26 (m, J = 7.0 Hz, 4H), 6.90 (m, J = 8.8 Hz, 4H), 5.03 (m, J = 6.6 Hz, 4H), 4.26 (m, J = 6.8 Hz, 6H), 3.91 (m, J = 5.6 Hz, 2H), 3.81 (s, 6H), 1.27 (t, J = 4.8 Hz, 3H) (Figure 5.42).

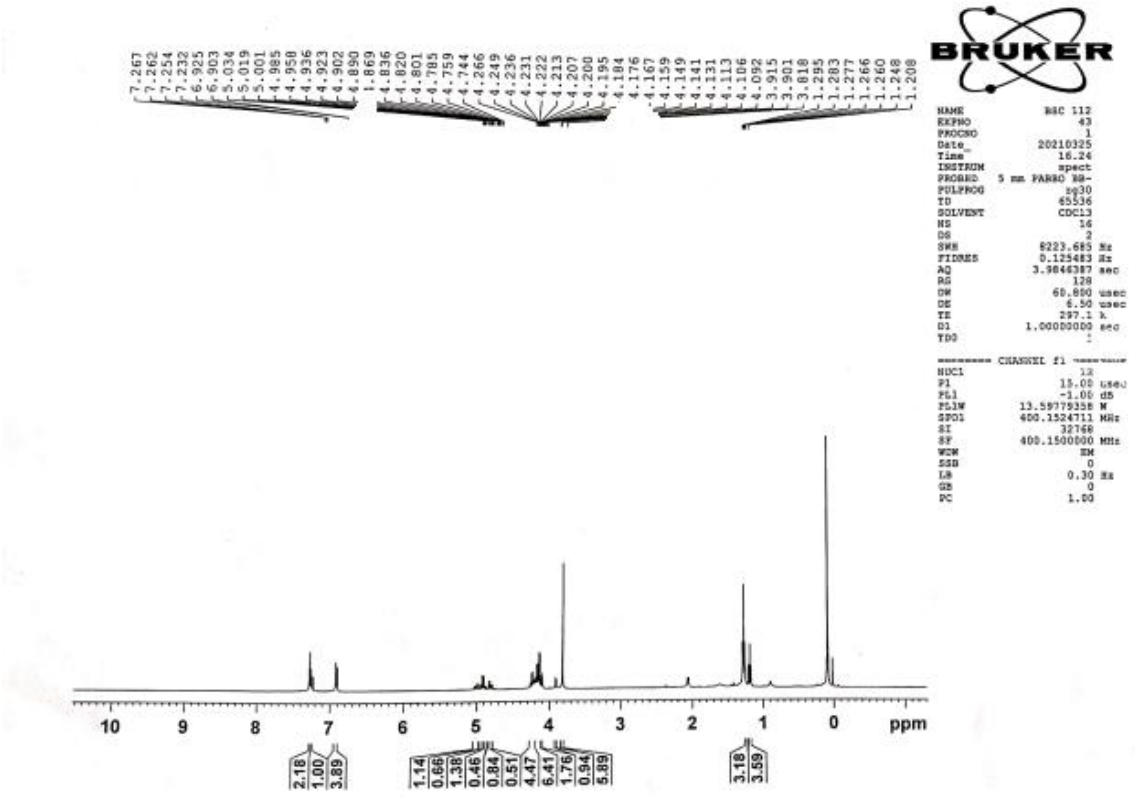

Fig. 5.42. ^{1}H-NMR spectra of the product (3c).

Ethyl 2-cyano-4-nitro-3(4-methylphenyl) butanoate (3d)

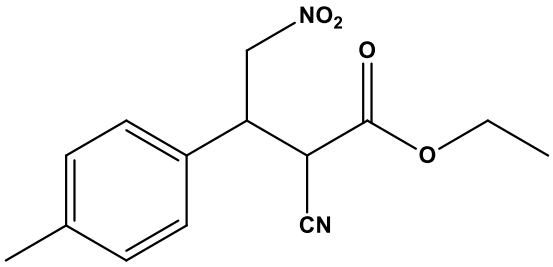

Colorless oil. ^{1}H NMR (400 MHz, $CDCl_3$) δ: 7.18 (m, J = 6.8 Hz, 8H), 5.04 (m, J = 6.4 Hz, 4H), 4.7 (m, J = 7.2 Hz, 6H), 4.27 (m, J = 6.8 Hz, 2H), 2.35 (s, 3H), 1.16 (t, J = 7.2 Hz, 6H) (Figure 5.43).

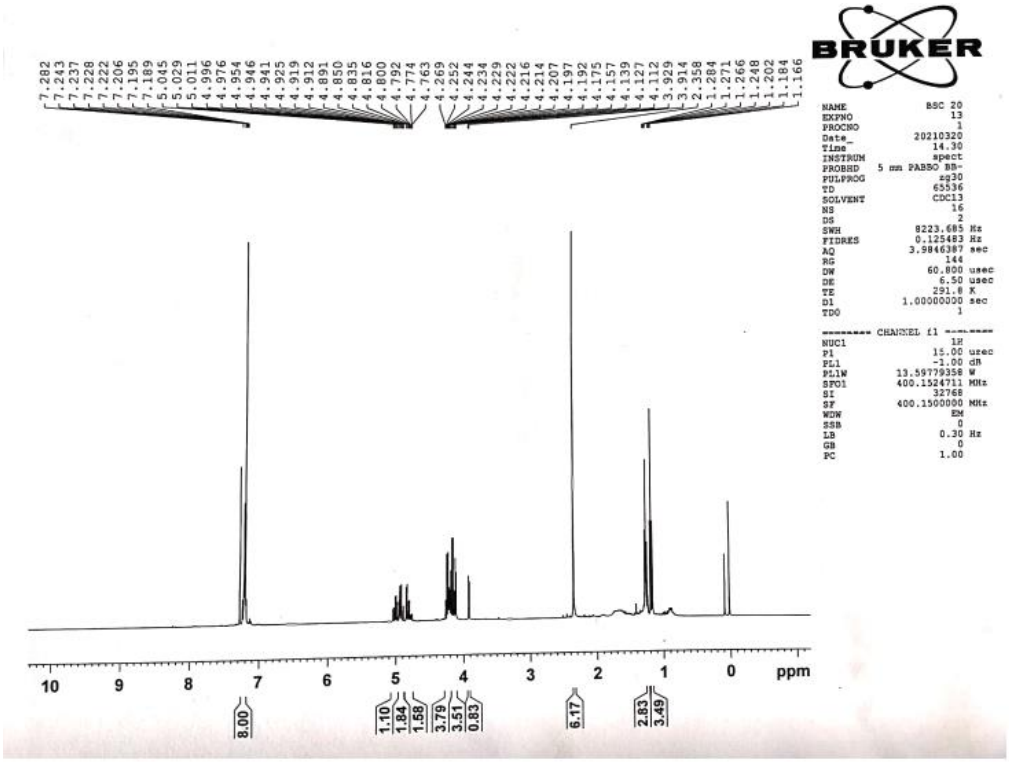

Fig. 5.43. ^{1}H NMR spectra of the product (3d).

5.9 References

1. M.P. van der Helm, B. Klemm, R. Eelkema, Nat. Rev. Chem. 3, 491 (2019).
2. S.E. John, S. Gulati, N. Shankaraiah, Org. Chem. Front. 8, 4237 (2021).
3. E. Heuson, F. Dumeigni, Catal Sci Technol. 10, 7082 (2020).
4. S. Khaef, A. Rostami, V. Khakyzadeh, M.A. Zolfigol, A.A. Taherpour, M. Yarie, Mol. Catal. 484, 110772 (2020).
5. A. Khazaei, A.R. Moosavi-Zare, F. Gholami, V. Khakyzadeh, Appl. Organometal. Chem. 30, 691 (2016).
6. V. Khakyzadeh, H. Rezaei-Vahidian, S. Sediqi, S.B. Azimi, R. Karimi-Nami, Chem. Methodol. 5, 324 (2021).
7. B. List, Chem. Rev. 107, 5413 (2007).
8. B. List, Angew. Chem. Int. Ed. 49, 1730 (2010).
9. P.I. Dalko, L. Moisan, Angew. Chem. Int. Ed. 43, 5138 (2004).
10. D. Elhamifar, S. Kazempoor, B. Karimi, Catal. Sci. Technol. 6, 4318 (2016).
11. L. Zhu, N. Lei, Z. Miao, C. Sheng, C. Zhuang, J. Yao, W. Zhang, Chin. J. Chem. 30, 139 (2012).
12. Y. Wang, Z. Shang, T. Wu, J. Fan, X. Chen, J. Mol. Catal. A. Chem. 253, 212 (2006).
13. A. Rahmati, K. Vakili, Amino Acids 39, 911 (2010).
14. J. Han, Y. Xu, Y. Su, X. She, X. Pan, Catal. Commun. 9, 2077 (2008).
15. P.S. Rao, R.V. Venkataratnam, Tetrahedron Lett. 32, 5821 (1991).
16. B. Green, R.I. Crane, I.S. Khaidem, R.S. Leighton, S.S. Newazand, T.E. Smyser, J. Org. Chem. 50, 640 (1985).
17. R.M. Kumbhare, M. Sridhar, Catal. Commun. 9, 403 (2008).
18. D.S. Bose, A.V. Narsaiah, J. Chem. Res. 1, 36 (2001).
19. M. Trilla, R. Pleixats, M.W.C. Man, C. Bied, Green Chem. 11, 1815 (2009).
20. K. Motokura, M. Tada, Y. Iwasawa, Chem. Asian J. 3, 1230 (2008).
21. R. Vaid, M. Gupta, Montash chem.146, 645 (2015).
22. M. Kolahdoozan, R.J. Kalbasi, Z.S. Shahzeidi, F. Zamani, J. Chem. 496837 (2013).
23. S. Kantevari, R. Bantu, L. Nagarapu, J. Mol. Catal. A: Chem 269, 53 (2007).

24. V.S.R.R. Pullabhotla, A. Rahman, S.B. Jonnalagadda, Catal. Commun. 10, 365 (2009).

25. P.M. Price, J. H. Clark, D. J. Macquarrie, J. Chem. Soc., Dalton Trans. 101 (2000).

26. J. Yu, L. Zhang, B. Cheng, Y. Su, J. Phys. Chem. 111, 10582 (2007).

27. A. Corma, S. Iborra, I. Rodriguez, F. Sanchez, J. Catal. 211, 208 (2002).

28. M.B. Gawande, R.V. Jayaram, Catal. Commun. 7, 931 (2006).

29. S. Saravanamurugan, M. Palanichamy, M. Hartmann, V. Murugesan, Appl. Catal. A. 298, 8 (2006).

30. A. Corma, R.M. Martin-Aranda, Appl. Catal. A 105, 271 (1993).

31. T.I. Reddy, R.S. Verma, Tetrahedron Lett. 38, 1721 (1997).

32. U.D. Joshi, P.N. Joshi, S.S. Tamhankar, V.V. Joshi, C.V. Rode, V.P. Shiralkar, Appl. Catal. A. 239, 209 (2003).

33. A. Corma, V. Fornes, R.M. M. Aranda, H. Garcia, J. Primo,Appl. Catal. 59, 237, (1990).

34. J. N. Appaturi, R. Ratti, B. L. Phoon, S. M. Batagarawa, I. Ud Din, M. Selvaraj, R. J. Ramalingam, Dalton Trans. 50, 4445 (2021).

35. K. Komura, Y. Mishima, M. Koketsu, Appl. Catal. A: General 445, 128 (2012).

36. E. Rodrigo, B.G. Alcubilla, R. Sainz, J.L.G. Fierro, R. Ferritto, M.B. Cid, Chem. Commun. 50, 6270 (2014).

37. H. Ishitani, K. Kanai, Y. Saito, T. Tsubogo, S. Kobayashi, Eur. J. Org. Chem. 6491 (2017).

38. R. Jenkins, R.L. Snyder, Introduction to X-ray Powder Diffractometry (John Wiley & Sons, NY, 1996).

39. E. Shah, H.P. Soni, RSC Adv. 3, 17453 (2013).

40. E. Shah E, P. Upadhyay, M. Singh, M. S. Mansuri, R. Begum, N. Sheth, H. P. Soni, New J. Chem. 40, 9507 (2016).

41. M. Kakihana, T. Nagumo, O. Makoto, H. Kakihana, J. Phys. Chem. 91, 6128 (1987).

42. P.S. Subramanian, P.C. Dave, V.P. Boricha, D. Srinivas, Polyhedron 17, 443 (1998).

43. G.B. Deacon, R.J. Philips, Coord. Chem. Rev. 33, 227 (1980).

44. T.F. Pauwels, W. Lippens, P.W. Smet, G.G. Herman, A.M. Goeminne, Polyhedron 18, 1029 (1999).

45. A. Barth, Prog. Biophys. Mol. Biol. 74, 141 (2000).

46. K.S.W. Sing, D.H. Everett, R.A.W. Haul, L. Moscou, R.A. Pierotti, J. Rouquerol, T. Siemieniewska, Pure Appl. Chem. 57, 603 (1985).

47. J. Chomoucka, J. Drbohlavova, D. Huska, V. Adam, R. Kizek, J. Hubalek, Pharmacol. Res. 62, 144 (2010).

48. L. Li, Y. Yang, J. Ding, J.M. Xue, Chem. Mater. 22, 3183 (2010).

49. H.L. Swanson, C. Guo, M. Cao, Phys. Chem. Chem. Phys. 22, 20349 (1998).

50. R.A. Sheldon, Green Chem. 19, 18 (2017).

51. D. Meng Y. Qiao, X. Wang, W. Wen, S. Zhao, RSC Adv. 8, 30180 (2018).

52. D. Patel, R. Vithalani, C.K. Modi, New J. Chem. 44, 2868 (2020).

53. G. Wang, Z. Ding, L. Meng, G. Yan, Z. Chen, J. Hu, Appl. Organomet. Chem. 34, 5907, (2020).

54. I. delHeirro, Y. Pérez, M. Fazardo, Mol. Catal. 450, 112 (2018).